UNIVERSIDAD NACIONAL AUTÓNOMA DE MÉXICO
POSGRADO EN CIENCIAS DE LA TIERRA
INSTITUTO DE GEOFÍSICA

NUMERICAL SIMULATION OF THE SUPER HOT GEOTHERMAL RESERVOIR AT LOS HUMEROS, MEXICO

T E S I S

QUE PARA OPTAR POR EL GRADO DE
MAESTRO EN CIENCIAS DE LA TIERRA

P R E S E N T A:
JOSÉ EDUARDO GRANADOS PASTRNA

Directora de Tesis
Dra. Rosa María Prol Ledesma
Instituto de Geofísica

Miembros del comité Tutor
Dr. Eric Morales Casique
Instituto de Geología
Dr. Ernesto Rubio Acosta
Instituto de Investigaciones en Matemáticas Aplicadas y en Sistemas

Ciudad Universitaria Cd. Mx. **Octubre 2020**

Agradecimientos

A Conacyt por el apoyo económico para estudiar esta maestría y realizar una estancia de investigación. Al Professor Michael John O'Sullivan quien me aceptó amablemente en la Universidad de Auckland y me enseñó a utilizar el código TOUGH2. A la Dra. Rosa María Prol quien me ha enseñado tanto, ha creído en mí y me ha motivado para enfocar mis esfuerzos en el campo de la geotermia. A mis profesores y amigos cuyas enseñanzas y apoyo siempre apreciaré. Y principalmente, agradezco a mis padres y hermanos quienes han luchado incansablemente para enseñarme principios y valores fundamentales que hoy han hecho de mi un ser humano que genera valor a la sociedad.

Abstract

This document highlights the importance of geothermal energy based on the analysis of historical data sets of economic investment and energy production, comparing these parameters with those of other renewable and conventional energies. In order to motivate development and research in this energy sector.

On the other hand, the principal aim of this paper was focused on calibrating a natural state model of Los Humeros Geothermal Field (LHGF). First, it was necessary to build a conceptual model which included all the main geological, structural, hydrological and geothermal features. This conceptual model was used as the basis of a numerical model with a Voronoi mesh design. The discretization of the model, included the geological units and the faults, with permeabilities ranging from 5.5e-13 m^2 to 8.2e-16 m^2, in order to represent both the faults which control the thermal manifestations and faults which work as hydrological barriers to host the geothermal reservoir.

A large number of simulations were processed to obtain a calibrated 3D Model, that achieved a good match to the distribution of temperature and water table levels, as well as a good representation of the groundwater flow. Finally, it is proposed to use this model in future works by setting up it with a supercritical EOS to achieve an improved calibration and then to perform production and reinjection simulations, selecting the best scenario in order to extend the useful life of the reservoir.

Resumen

Este documento destaca la importancia de la energía geotérmica basado en el análisis de un conjuntos de datos históricos de inversión económica y producción de energía, comparando dichos parámetros con los de otras energías renovables y convencionales. Con el fin de motivar el desarrollo y la investigación en este sector energético.

Por otro lado, el objetivo principal de este trabajo se centró en la calibración de un modelo de estado natural del Campo Geotérmico Los Humeros (LHGF). Primero, fue necesario construir un modelo conceptual que incluyera todas las características geológicas, estructurales, hidrológicas y geotérmicas principales. Este modelo conceptual se utilizó como base de un modelo numérico con un diseño de malla Voronoi. La discretización del modelo incluyó las unidades geológicas y las fallas, con permeabilidades que van desde 5.5e-13 m^2 a 8.2e-16 m^2, para representar tanto las fallas que controlan las manifestaciones térmicas y fallas que funcionan como barreras hidrológicas para albergar el reservorio geotérmico.

Se procesó una gran cantidad de simulaciones para obtener un Modelo 3D calibrado, que logró un buen ajuste con la distribución de los niveles de temperatura y nivel freático, así como una buena representación del flujo subterráneo. Finalmente, se propone utilizar este modelo en futuros trabajos configurándolo con un EOS supercrítico para lograr una calibración mejorada y luego realizar simulaciones de producción y reinyección, seleccionando el mejor escenario para extender la vida útil del yacimiento.

Contents

List of Figures

Chapter 1

Introduction

Due to the growing energy demand and the need to reduce greenhouse gases emissions, there has been a great growth in the use of renewable energy. One of these is Geothermal Energy which at the end of 2006 was reported to produce up to 35 times less CO_2 for each MWh compared to that produced by coal (Slack, 2009). By 2016, Geothermal energy contributed 1.9% of the total electrical capacity installed worldwide (Global-Energy-Observatory, 2018). Despite the fact that historically it has been allocated up to 5 times less investment than "Biomass and Waste", 37 times less than the "Solar" and 250 times less than the "Wind", geothermal energy has shown the most stable annual growth rates and by the end of the same year showed the highest growth rate (17.4%) compared to other renewable energies, based on the Compounded Annual Grow Rate calculated for data taken from Ritchie and Roser, 2020. Due to the above it is essential to continue research and development of new technologies and models which satisfactorily reproduce the main characteristics of geothermal fields. This research will help to achieve a more efficient exploitation and prolong the useful life of the geothermal fields, in order to obtain greater profitability and achieve greater financial investments in this energy sector.

This thesis is mainly focused on the construction and calibration of a natural state model of Los Humeros Geothermal Field (LHGF), through the design of a 3D Numerical Model, which describes the heat and mass flow in the geothermal field in steam and liquid phases. The simulations assume a multicomponent system (air and water, using EOS3, see Pruess et al., 1999) and use the AUTOUGH2 code (University of Auckland's version of the TOUGH2 code).

To develop such a 3D numerical model, first a conceptual model was made which included the main geological units and structures, temperature distribution, superficial manifestations and knowledge about the recharge and discharge zones. The conceptual model was built with LeapFrog software, then it was discretized with a Voronoi mesh designed with the AMESH code (Haukwa, 1998) and the PyTOUGH library. PyTOUGH (Croucher, 2018) was set up to help set up models and manage simulations with the AUTOUGH2 simulator.

The calibration required the modification of petrophysical properties of the geological units as well as the adjustment of the boundary conditions. The natural state model calibration was based on achiving a good match between the temperature

resulting from the simulation and the temperature logs published by CFE.

The first section of Chapter 2 discusses the historical geothermal energy production in the world, its low CO2 generation compared with conventional energies, as well as the financial investment dedicated over the past 15 years, through the use of Python and Tableau software to do some calculations and display the visualizations. The second section, also describes the main features of LHGF such as geological units and structures, principal fluid composition, petrophysical properties and production history. Chapter 3 discusses the importance of modelling, the data required to perform a simulation of a geothermal reservoirs, how the numerical model is calibrated and validated. The main mathematical theory behind reservoir simulation, as well as a description of the simulator used (TOUGH2) in this work. Chapter 4 shows how all the main features of LHGF are integrated into a 3D conceptual model and how it is transformed into a numerical model to be used in AUTOUGH2. Finally Chapter 5 discusses the results of the calibration of the natural state and production models.

Chapter 2

Background

This chapter comprises of 2 main sections, the first of which analyzes the increase in energy demand and the concern about the reduction of greenhouse gases, and how these needs have opened the way for different renewable energies. Throughout this section, the production, financial investment and the compounded annual growth rate will be graphically analyzed (calculations and visualizations made with Python and Tableau software). In the second section, the main features of Los Humeros Geothermal Field are discussed.

2.1 The Global Energy

Between 1850 and 2006, the world population increased from about 1.3 billion to about 6.5 billion, an increase of five times. Current estimates are that, between the years 2000 and 2050, the population will grow from about 6.1 billion to about 8.9 billion, an increase of 47% in 50 years (United-Nations, 2004). On the other hand, the average per person energy consumption between the years 1850 and 2006 increased from about $4.85x10^9$ $J/person/yr$ to over $76.2x10^9$ $J/person/yr$, an increase of more than 15 times. In other words, not only is the population of the planet growing rapidly, the average person is using more energy each year than they used previously (US-Energy-Administration, 2008). An additional issue that has taken on importance is the environmental impact of fuel extraction and energy use. There now is little scientific debate that the use of carbon-based fuels for energy generation has affected the atmosphere and with it the global climate (Solomon, Qin, Manning and Chen, 2007). Carbon-based fuels and human activity produce gases such as carbon dioxide (CO_2), oxides of nitrogen and methane (CH_4), among others, all of which affect the ability of the atmosphere to absorb or transmit radiation. As the abundance of these greenhouse gases increases in the atmosphere, the transmissivity of the atmosphere to thermal energy drops. The result is an increase in the average surface temperature of the planet. Between 1850 and 2006 total emissions of CO_2 to the atmosphere from human activity increased from $5.4x10^{10}$ kg/yr to $8.23x10^{12}$ kg/yr. This change represents an increase of more than 152 times (US-Energy-Administration, 2008).

Civilization has developed three main sources of non-renewable energy. The most

commonly used source includes the fossil fuels namely: coal, oil, and natural gas. While the principal types of renewable energy are, in order of decreasing energy contribution, hydroelectric, wind, solar photovoltaic waste-biomass and geothermal.

2.1.1 Geothermal energy as a renewable energy source

Throughout history, energy sources such as coal, gas and oil have been used to produce energy. It was not until the middle of the last century that renewable energy began to have a greater presence, mainly hydroelectric energy (Figure 2.2), which by 2017 represented more than half of total renewable energy. And for the same year, geothermal energy only contributed 1.87% (Figure 2.1). However since 1958 this energy source has always shown positive annual growth rate and at an average of 8% (Figure 2.4).

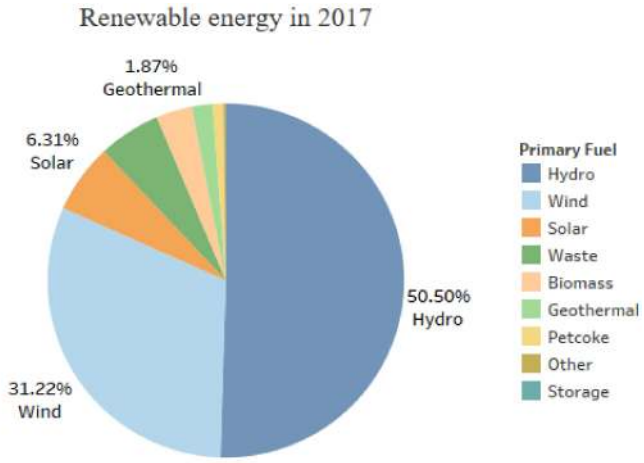

Figure 2.1: Renewable energy production in 2017. Dataset taken from Global-Energy-Observatory (2018).

There has been a growing interest in reducing dependence on fossil fuels, using alternative energies that can reduce or eliminate the production of greenhouse gases. According to Glassley (2015), the criteria that are generally used to establish the viability of an energy source that would supplant or displace dependence on fossil fuels are:

- It is sufficiently abundant to meet a significant percentage of the market demand.
- It can be obtained at a cost competitive with existing energy sources.
- Its use will reduce or eliminate greenhouse gas emissions.
- It is self-replenishing (i.e., renewable).

One energy source that meets all these requirements is geothermal energy, which has an inexhaustible source of energy due to the flow of heat from the Earth's interior,

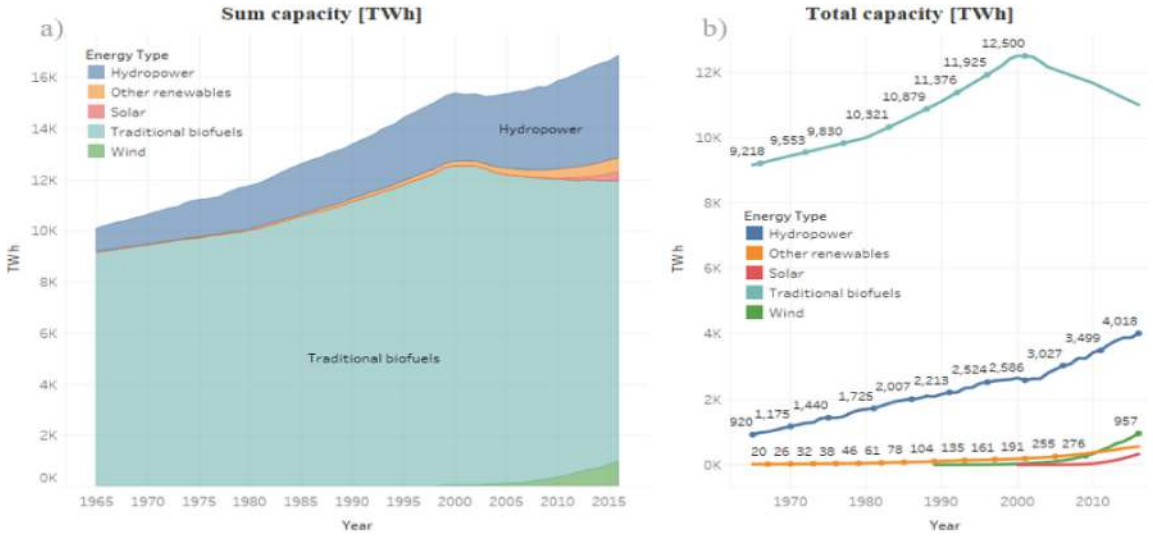

Figure 2.2: : Historical energy capacity since 1965 to 2016. a) Total historical energy capacity since 1965 to 2016. b) How much each energy type has contributed. Dataset taken from Ritchie and Roser (2020).

and results in greenhouse gas emissions that are significantly lower than conventional energies. For example, the CO2 emission produced by the flash geothermal plant is approximately 35 times less than for a coal fired plant (Figure 2.3). Another significant attribute is that geothermal heat occurs in diverse ways, making it possible to use it for different purposes. It can be used as a source of energy for heating, ventilating and air conditioning. Other direct use applications include: food processing, drying materials, agricultural activities and greenhouses, aquaculture, paper manufacturing, among others. Commercial exploitation of the geothermal resource started at 1904 in Larderello, Intaly, with an installed capacity of 10 kWh, by 2017 the total world geothermal energy capacity installed has reached 12,715 MWh (Figure2.4b).

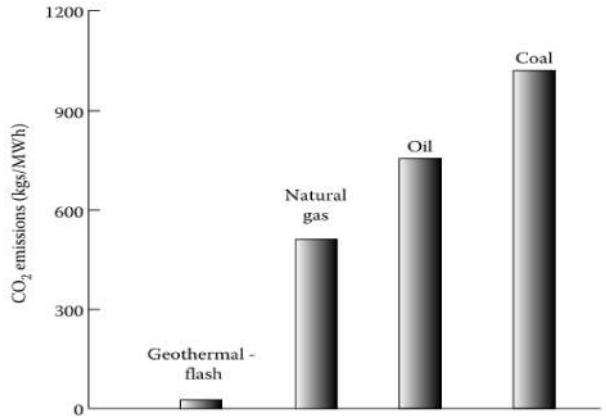

Figure 2.3: CO_2 emissions (in kg of CO_2/MWh) for different power generating technologies. The values for the generating systems that use fossil fuels are from the U.S. Environmental Protection Agency eGrid 2000 database. The data for geothermal power technologies is from Slack (2009). Binary geothermal power generation produces no emissions (Slack, 2009).

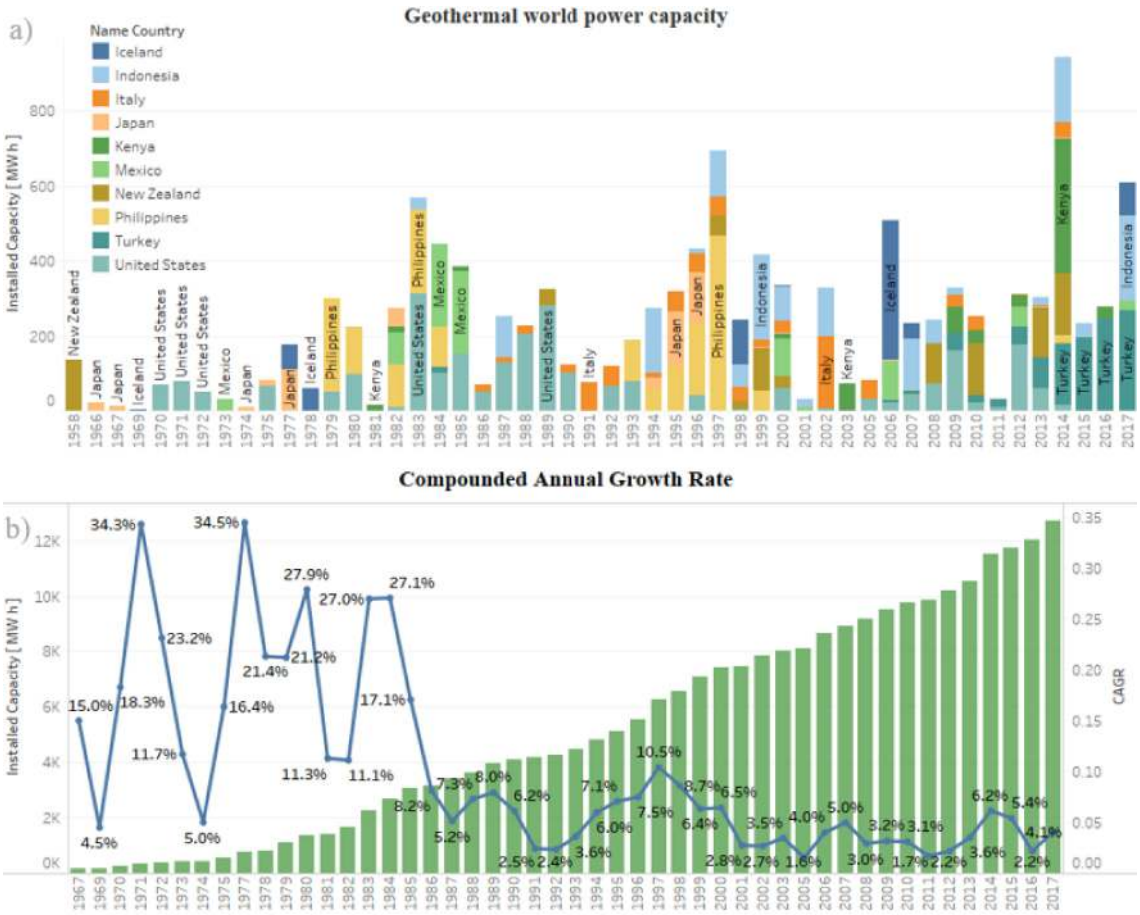

Figure 2.4: a) Historical installed capacity of the top 10 geothermal energy providers each one in different color. b) The green bars are showing the worldwide geothermal capacity sum, while the blue line represents Compounded Annual Grow Rate. Dataset taken from Uihlein (2018) and Global-Energy-Observatory (2018).

Throughout history geothermal energy has shown constant growth and positive annual growth rates (Figure 2.4). For example, it has shown great stability against energies (Figure 2.5) such as Biomass Waste and Biofuels, which show significant reductions in its budget. Annual growth from 2005 to 2015 (Figure 2.5) averaged -1.6% for "Biofuels" and 1% for "Biomass and Waste", while investment in geothermal energy showed an average annual growth of 14.5% similar to the growth of energy wind power, although with 500 times less budget. That is why it is important to relate total production to economic investment.

As can be seen in the Figure 2.6, wind energy has had an increasing economic investment, reaching more than 124 Billion dollars in 2015, and achieving productions of up to 950TWh, while together, energies such as waste, biomass and geothermal show a maximum investment in 2007 corresponding to less than half of the investment in wind energy in 2015. After 2007, economic investment in geothermal reduced, as has been seen previously, mainly in Waste and Biomass. But despite this, renewable energy production has been growing constantly, thanks to energies such as geothermal.

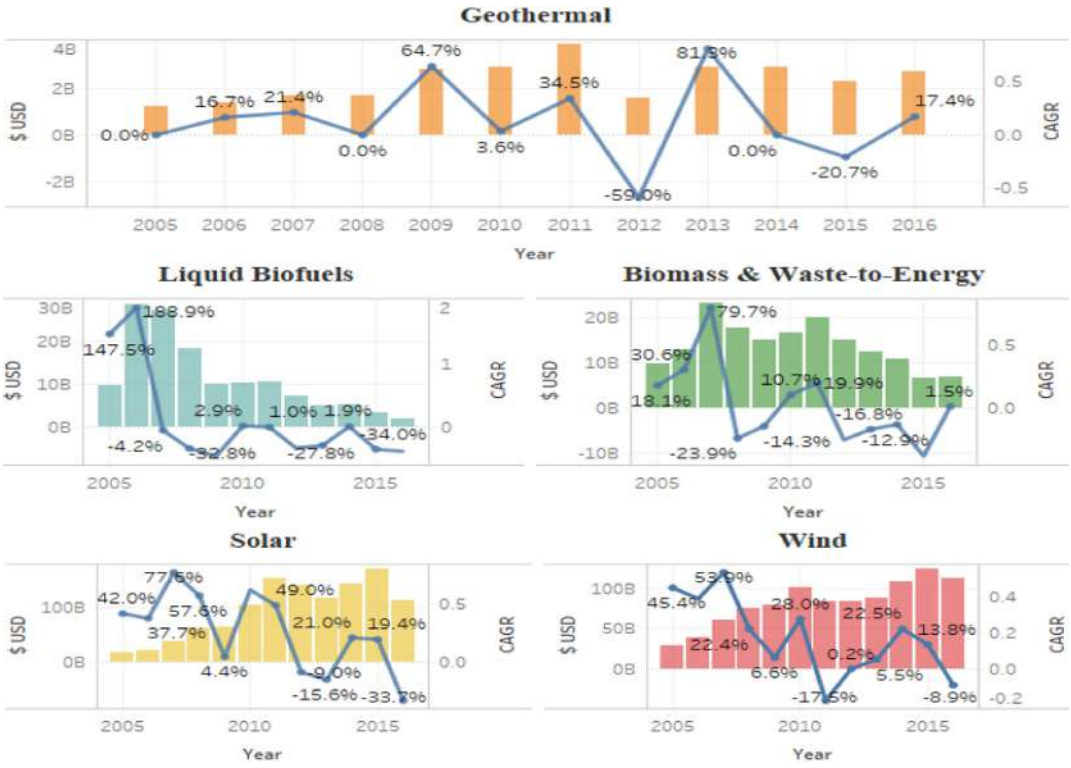

Figure 2.5: Total investment since 2004 to 2016. The blue line represents the Compounded Annual Growth Rate (Dataset taken from Ritchie and Roser, 2020).

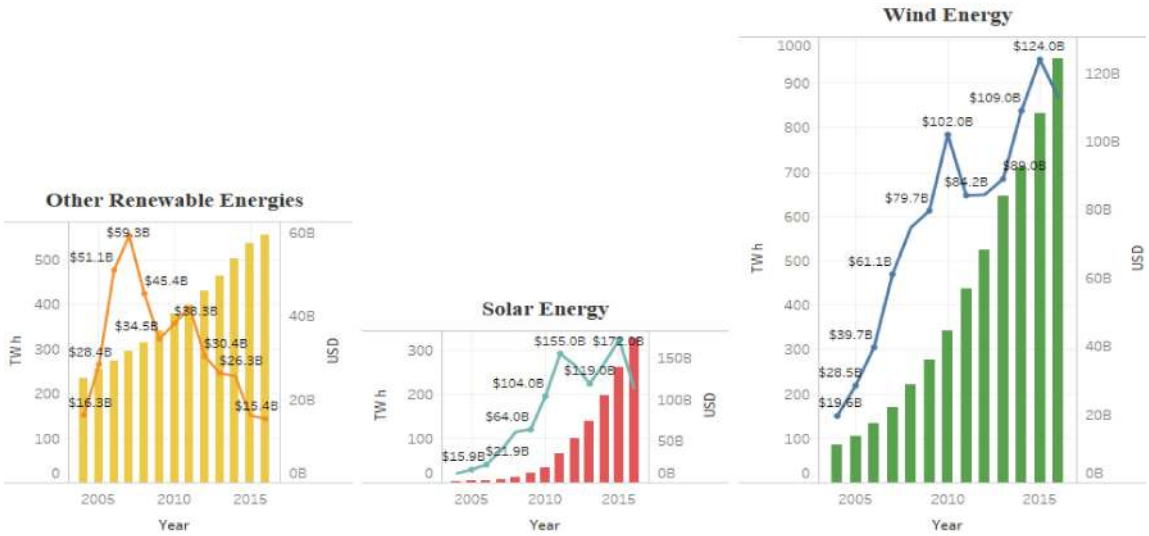

Figure 2.6: Bar charts represent the total energy production since 2004 to 2016. The lines represent the Compounded Annual Grow Rate for economic investment (Dataset taken from Ritchie and Roser, 2020).

2.2 Los Humeros Geothermal Field

Los Humeros Geothermal Field (LHGF), located in the eastern sector of the Trans-Mexican Volcanic Belt (TMVB), is the third most important geothermal field in Mexico, with an installed capacity of 94 MW in 2017 (Figure 2.7). LHGF production started in 1991, and over the years 8 back pressure units were installed (the last in 2008). Then in 2012, 2013 and 2017 a single flah unit was installed in each year and the back pressure units were decommissioned. The first well was drilled in 1981 and by 1999 there were 40 wells (Figure 2.8). According to Carrasco-Núñez, Hernández and De-León (2017) nowadays there are about 50 wells drilled and around 20 producing wells.

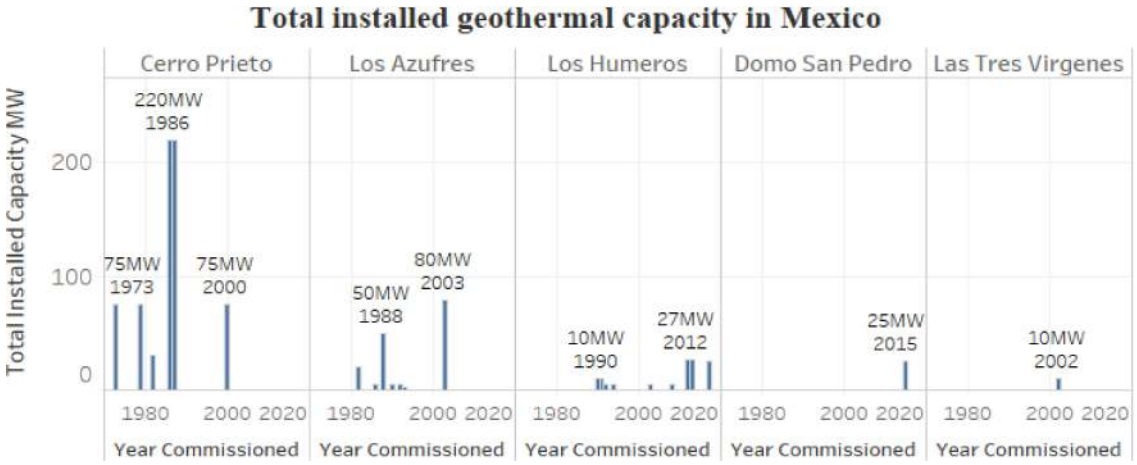

Figure 2.7: Geothermal power plants installed in Mexico, showed in descendent order from left to right, as well as the year when each new unit was commissioned. The data-set was taken from R. and Maya-González (2015) and Flores-Armenta (2017).

Twenty-six years of exploitation have caused boiling, phase separation, and condensation, while the effect of used geothermal fluid reinjection is still unclear (Arellano et al., 2015). Planning of future geothermal exploitation must be based on a clear understanding of fluid circulation within the system. Although numerous studies on the geology, as well as on the fluid geochemistry have been carried out, several questions remain unanswered. Some of the most relevant, concerning the dynamics of this geothermal system include: a) whether LHGF consists of two reservoirs or of one fed by different production zones (e.g., Gutiérrez-Negrín and Izquierdo-Montalvo, 2010) b) What is the origin of the very acidic fluids deeper in the main productive northern zone is (Izquierdo-Montalvo and Gutiérrez-Negrín, 2009); and c) the extent of recharge and the location of the contributing areas. The last query can be explained by considering the water table levels, a topic discussed below.

2.2.1 Geologic and structural settings

The basement rocks of the LGHF are granites and schists of Paleozoic age, covered by a thick series of Jurassic and Cretaceous limestones, metamorphosed during the

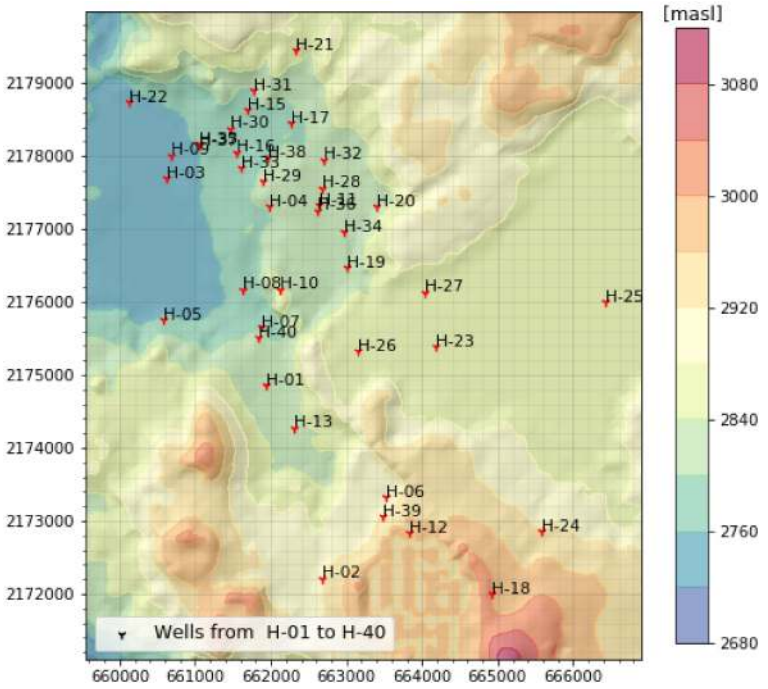

Figure 2.8: Digital Elevation Model and the forty wells drilled until 1999. Data reported by Castillo-Hernández (1999).

Laramide orogeny and by Oligocene magmatic intrusions (De la Cruz, 1983). Fissural volcanic activity in the area started in the Miocene (10 Ma), producing the Alseseca Andesites that outcrop in the northeastern part of the Los Humeros caldera. Further volcanic activity did not take place until the Pliocene, when the volcanism associated with the Mexican Volcanic Belt started, producing the Teziutlán Andesites in the area(3.5–1.9 Ma ago, Yáñez García and Casique-Velázquez, 1980) showed in Figure 2.9.

Los Humeros caldera formation started 460 ka ago, when a highly differentiated magmatic chamber was emplaced beneath the Mesozoic calcareous sequence. This process continued until 20 ka ago, ultimately leading to two nested calderas (Los Humeros and Los Potreros, Figure 2.10), and several rhyolitic domes and basaltic-andesite volcanoes within them. The largest caldera, which formed 460 ka ago following an eruption of $115 km^3$ of rhyolitic ignimbrites (Xaltipan Ignimbrite), has a diameter of 21 km (Ferriz and Mahood, 1984). Since this last major explosive episode, between 360 and 240 ka ago, several rhyolitic domes and rhyodacitic-andesitic plinian deposits were emplaced. At 100 ka, andesitic to rhyodacitic ignimbrites with an equivalent magma volume of 20 km^3 erupted, creating a new collapsed area inside the Los Humeros caldera. This collapse, called Los Potreros, has a diameter of 7–10 km. Finally, volcanic activity ended 20 ka ago with basaltic and andesitic lava flows, several scoria cones, and some phreato-magmatic explosions (Ferriz and Mahood, 1984). Since then, a geothermal system has been active, the heat source of which is the magmatic chamber at the terminal hydrothermal stage (Gutiérrez-Negrín and Izquierdo-Montalvo, 2010). A third depressed area,inside the Los Potreros caldera,

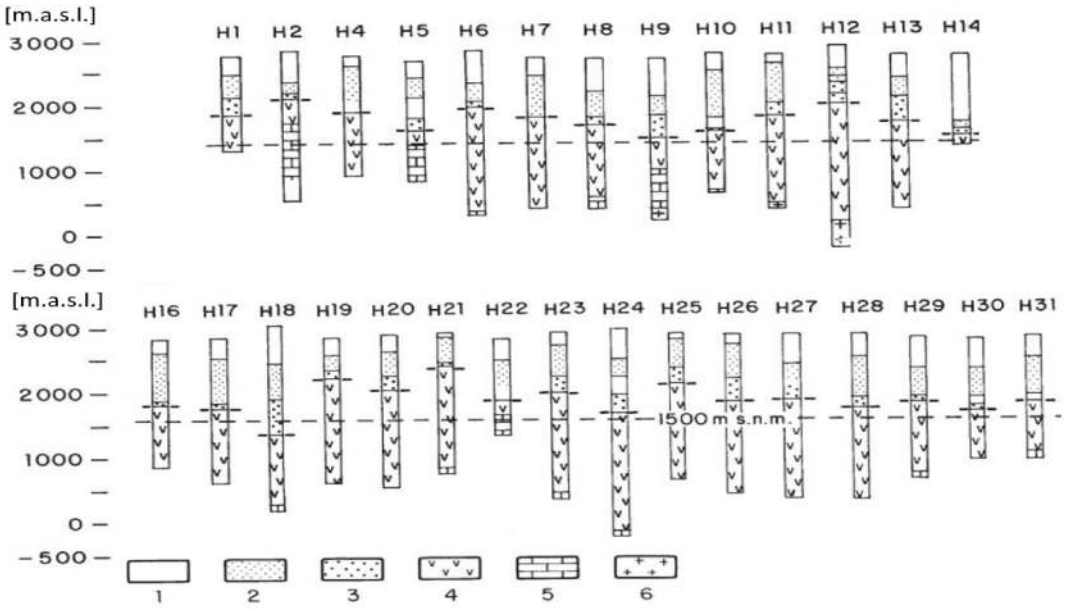

Figure 2.9: Lithologic columns of Los Humeros Wells, which shown the litologic units. 1.- post-caldera volcanism, 2- Xaltipan Igninmbrite, 4.- Teziutlan Andesite, 5.-Mosozoic limestone, 6.- granitic intrusive (González-Partida and Barragán-R., 1993).

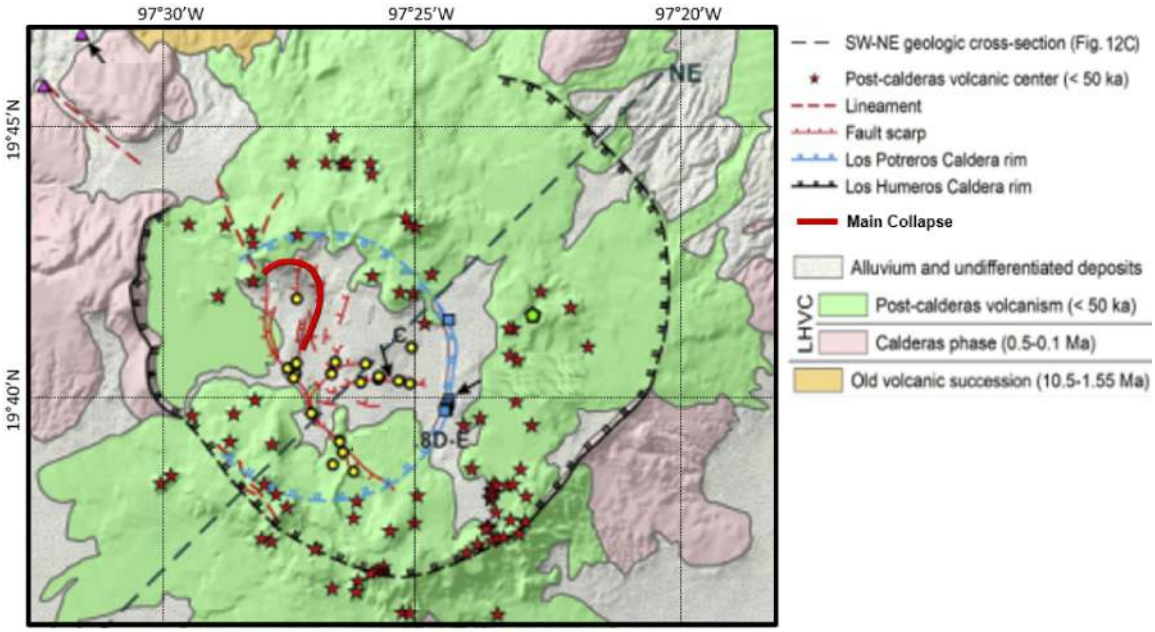

Figure 2.10: Principal structures and superficial geological units pre and post Los Humeros Caldera formation (Norini et al., 2015).

called the Main Collapse (Figure 2.11) and currently corresponding to the main productive geothermal area, is likely a morphological arrangement of lava flows rather than a volcanic caldera (Garduño-Monroy and Romero-Ríos, 1985). The geothermal reservoir of the Los Humeros system consists of a sequence of blocks surrounded by

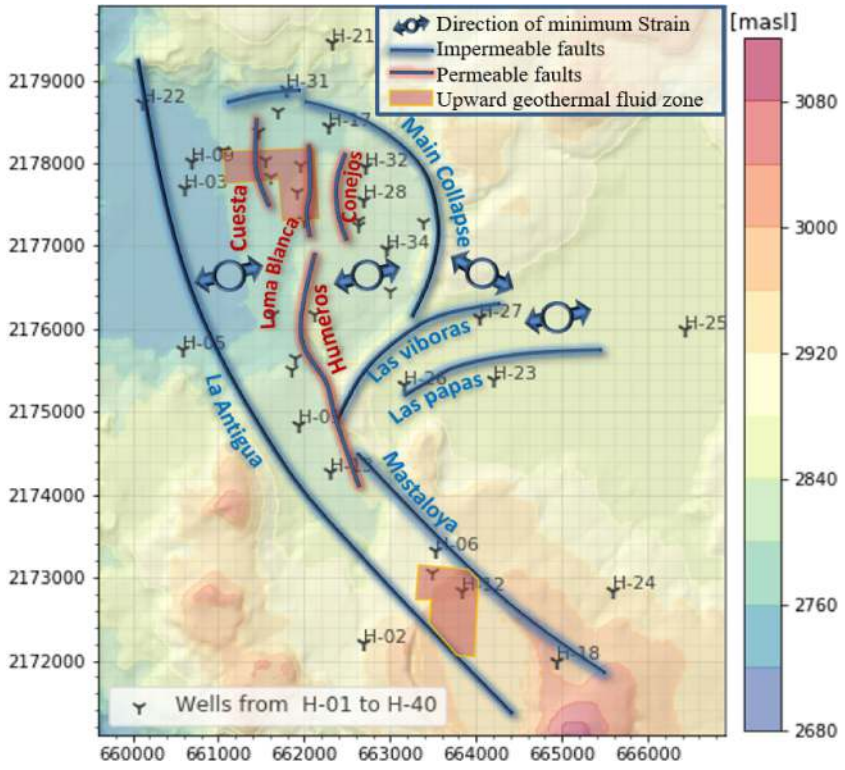

Figure 2.11: Main strain directions, faults and structures of Los Humeros Geothermal Field, reported by López-Hernández (1995). As well a as the outflow zones reported by Viggiano-Guerra and Robles-Camacho (1988).

fractures and faults arranged as graben and horst and associated with the collapse process of the Los Humeros Caldera formation (Figure 2.10). Two main structural systems, consisting of normal faults, are visible in the field (Figure 2.11): the oldest one has a NE-SW to E-W direction, such as the Las Papas fault; the younger one is a set of NW-SE to N-S normal faults, such as the Maztaloya, Los Humeros, and La Antigua faults, some of which cross-cut faults from the older system (Garduño-Monroy and Romero-Ríos, 1985). The La Antigua fault is an old basement structure, which was later reactivated and defines the western limit of the reservoir.

2.2.2 Hydrology

The well data has shown the presence of two aquifers limited by a fault systems and hosted in basalts, tuffs and andesites, whose lower limit is Xaltipan ignimbrite, and the lateral limits are Los Potreros caldera, La antigua fault and the main collapse, which act as hydrological barriers (Figure 2.11 and 2.12). The recharge is produced mainly by pluvial precipitation, while the main discharge occurs by faults at lower levels, (Castillo-Hernández, 1999). Using a Dataset of water table levels (CONAGUA, 2016) and geothermal wells in the field (Castillo-Hernández, 1999) a map was interpolated (Figure 2.13) then it was clipped, to show the LHGF area clearly and it was concluded that the groundwater recharge comes from West and East zones while the discharge

is mainly to the South-East, South and North zones.

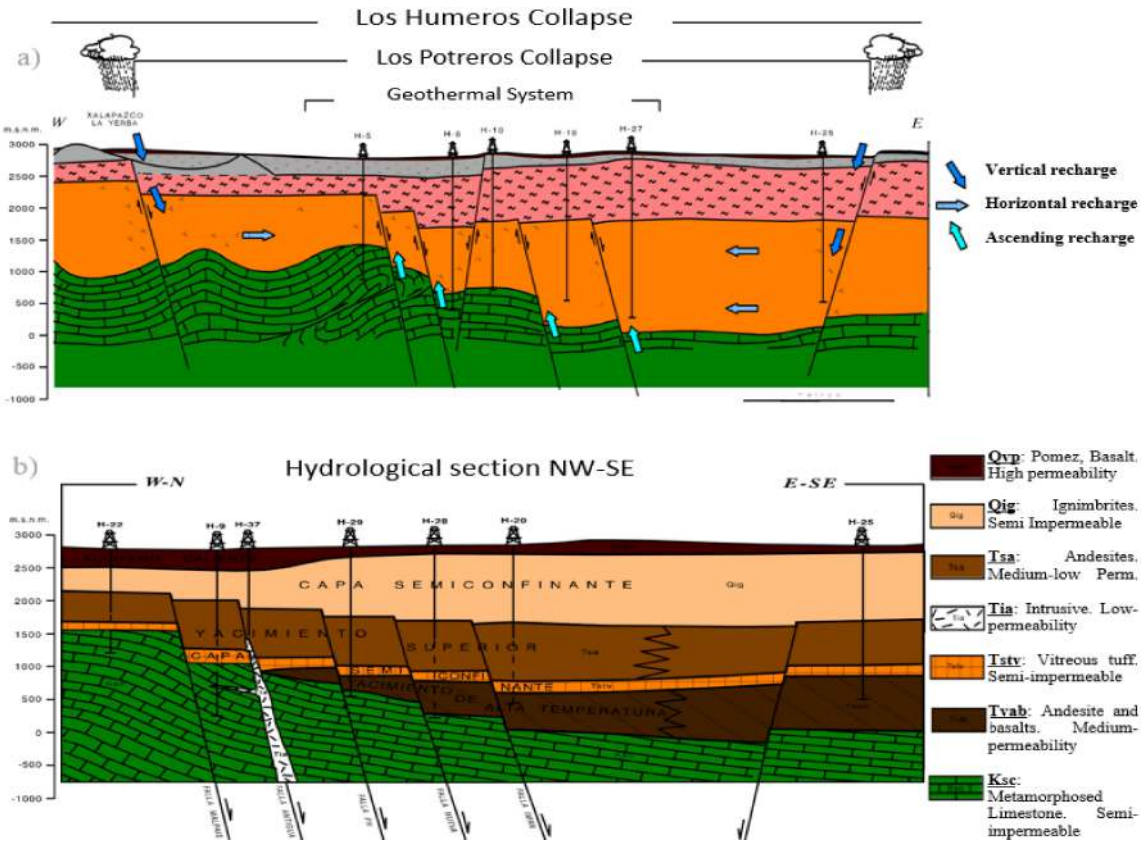

Figure 2.12: a) Regional hydrological model, diplayings the recharge zones as groundwater flow. b) Geological model which shows the two geothermal reservoirs and rock types.(Castillo-Hernández, 1999).

2.2.3 Geothermal features

According to Viggiano-Guerra (1988) LHGF has geothermal fluids reaching 400°C in the northern production area and production enthalpy higher than 2400 kJ/kg, but unfortunately it is characterized by a low-permeability (3E-14 m^2). Hence in order to define the geothermal reservoir limits Viggiano-Guerra and Robles-Camacho (1988) carried out an analysis of the geothermal fluid ascent zones based on the spatial distribution of autogenic minerals (Figure 2.14). The comparative configurations of two pairs of hydrothermal minerals: biotite vs wairakite (present in the southern and northern zones) and garnet vs wairakite (present only in the northern zone) demonstrate the interdependence of the geothermal upflow zones. The elongated NE-SW shape that these configurations describe is, therefore, the morphology of the reservoir and it follows that it is a response to the structures in which the system is hosted. Assuming an approximate thickness of 1000m for the producing aquifer, a volume of 16.3km3 was calculated (Viggiano-Guerra and Robles-Camacho, 1988).

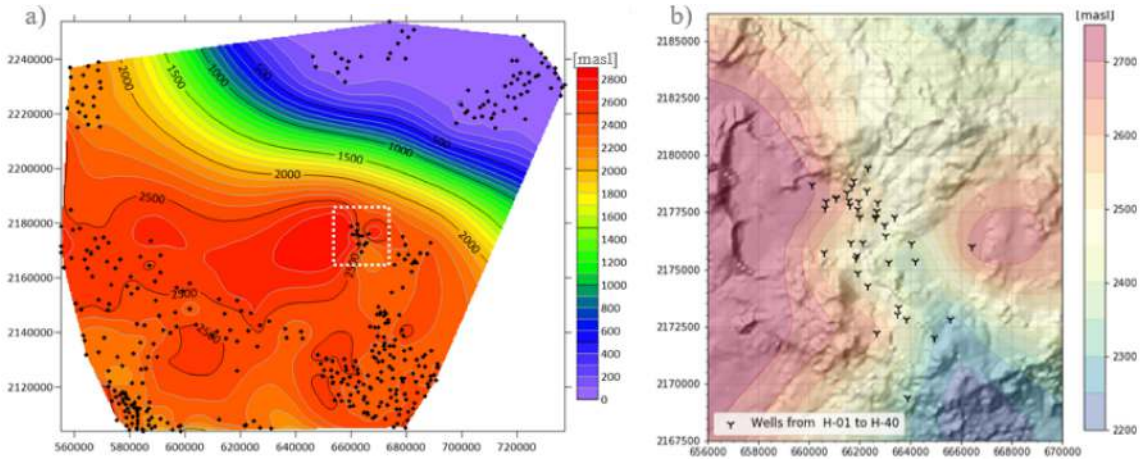

Figure 2.13: Water table level interpolated with minimum curvature method, the black points represent the information available and the white rectangle shows LHGF area. b) the map shows the water table level in LHGF with higher spatial resolution. Water table Datasets taken from CONAGUA (2016) and Castillo-Hernández (1999).

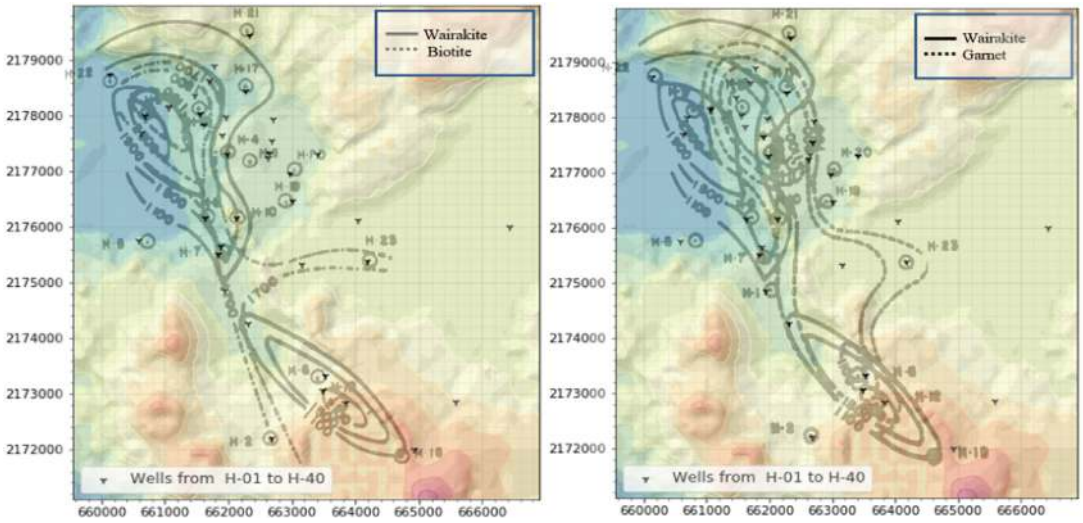

Figure 2.14: Configuration of the first ocurrences of wairakite (North: 1100 to 2000masl; South: 1010 to 2100) vs biotite (North: 1700 to 1900masl; South: 1700masl) and wairakite vs garnet (North: 900 to 1100masl). Viggiano-Guerra and Robles-Camacho (1988).

The temperature logs (Figure 2.15; Torres-Rodríguez, 1992; Izquierdo-Montalvo et al., 2008; Díaz, 2018) were used to identify the limits of the two reservoirs and to define them more precisely in the conceptual model. There are 3 principal patterns in the geothermal reservoir: the first (Figure 2.15a) going from the Central to the North and North-West zone where two reservoirs are clearly distinguished, the upper is in the range from 2000 to 1200m.a.s.l. and the top of the lower reservoir is at about 1000m.a.s.l. The second configuration in the reservoir (Figure 2.15b), reddish curves)is present mainly in the North and North-East zone where there is a continuous reservoir exhibiting convective behavior below 2000m.a.s.l. The last pattern in the

field (Figure 2.15b), green and blue curves) correspond to the wells which are the furthest from the geothermal reservoir, for example H-14, 21, 23, 24, 26, 27, which show the lowest temperatures as well as conductive profiles.

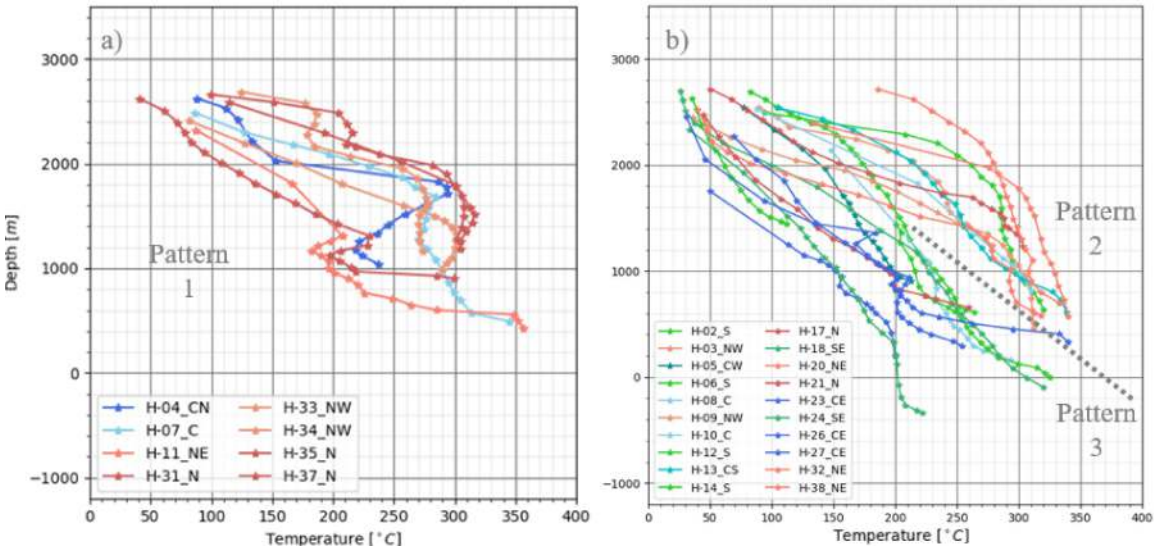

Figure 2.15: The color curve represents different zone in geothermal field. a) The upper and lower reservoirs can be distinguished. b) The dotted line separates the two remain reservoir patterns. The pattern 2 shows a continuous convective reservoir from 2000 to more than 1000m.a.s.l., while the pattern 3 has a conductive behavior and a unique lower reservoir below 800m.a.s.l.

2.2.4 Production and injection history

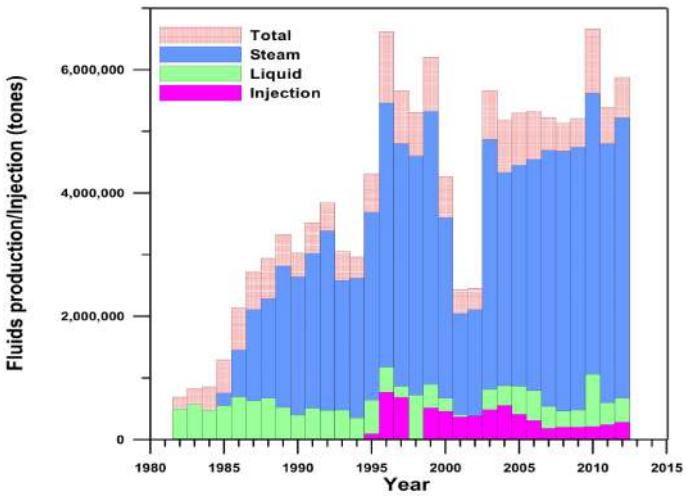

Figure 2.16: Fluids produced and injected in LHGF (Arellano et al., 2015).

LHGF history production can be analyzed from Figure 2.16 which shows how the production has been dominated by steam (except in H-01). The commercial

production started in 1991 but the first well H-01 started to produce in 1981. While the re-injection started since 1995 (the injector wells until 2012 were H-13, H-28, H-29, H-38 and H-40). The amount of fluids produced up to December 2012 was 122,934,290 tonnes, including 103,678,826 tonnes of steam (84.3 %) and 19,255,464 tonnes of water (15.7 %). Some of the fluids were injected back to the reservoir in order to minimize environmental impacts and also to provide recharge to the aquifer. From 1995 to December 2012, the amount of fluids re-injected to the reservoir was 6,301,863 tonnes (5.1%) (Arellano et al., 2015).

2.2.5 Geochemistry and isotopic data

In Figure 2.17 (right side) is shown a spatial distribution of the different LHGF zones for analyzing the distribution of the principal ions (Na, K, Ca, Mg, Cl, SO_4 and HCO_3), in order to know the zones with the highest content of chlorides and sodium (related to the geothermal reservoir) and higher carbonate and sulfate content (related to recharge areas).

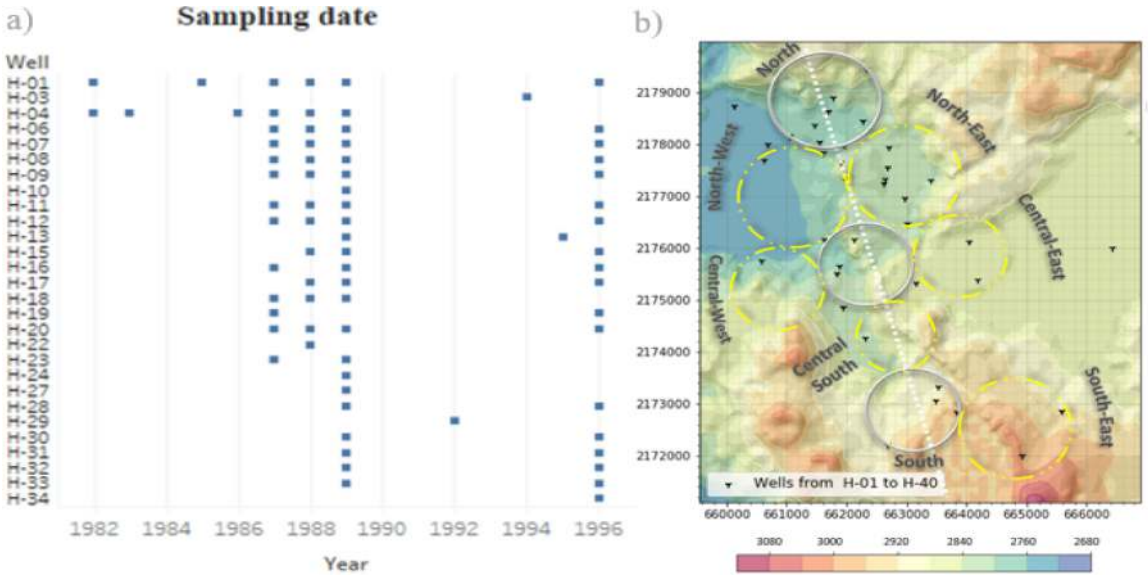

Figure 2.17: a) Sample dates of available geochemical information Viggiano-Guerra and Robles-Camacho (1988), Tello-Hinojosa (1992) and Castillo-Hernández (1999). b) Spatial division, in order to achieve a better classification of the fluids.

The reconstruction of the chemical composition of the fluid at reservoir conditions has been complicated since most wells present the phenomenon of "excess enthalpy" or "excess steam" (Barragán, Santoyo and Nieva, 1989). Another phenomenon that hinders this transmission is the occurrence of fluid mixing processes when the wells feed the two producing strata (Barragán et al., 1989). To check the ionic balance in LHGF fluids, 70 well samples were analyzed (Figure 2.17) and visualized through a ternary diagram (Figure 2.18) which shows the relative concentration of some ions based on Giggenbach (1988) and showing a ionic equilibrium only in 8 samples. In order to understand the chemical classification of the fluids, based on their relative

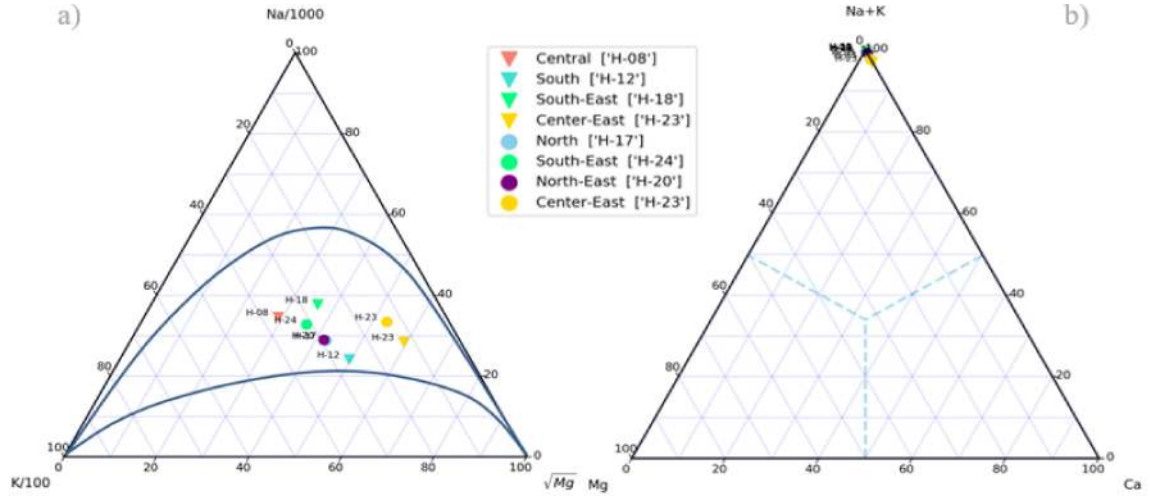

Figure 2.18: a) Only 8 samples out of 70 had a error lower than 10% in ionic balance (triangles are samples from 1987 and circles from 1989). The data between blue lines are in total equilibium, Based on Giggenbach 1988. b) Cations proportion contained in the fluid sampled.

Figure 2.19: Concentration of principal anions (Cl, HCO_3 and SO_4).

concentration, it was planned to produce two ternary diagrams showing the principal cations and anions proportion, but to show more clearly the concentrations in the different classified zones (Figure 2.17) three bar charts were produced (Figure 2.19). They show how, over the years, the concentration of chlorides has been reduced (comparing 1987 with 1996), probably due to exploitation, which reduces the water

table level, pulling in the adjacent waters (increasing the concentration of HCO_3 and SO_4). This make sense as in the North-West and South zones, each of which has less than 5 wells, still in 199 have a high chloride concentration compared to the rest of the areas (Figure 2.19). On the other hand the cations analysis (1987, 1989 and 1996) shows a predominant concentration of Na, K, as shown in Figure 2.18a, which summarizes the classification of sodium-chlorinated fluids before 1991 (before commercial exploitation).

Since 1987 isotopic analysis of Oxygen-18 and deuterium have been used to characterize the deep steam (38 to 58% andesitic water, Arellano, García and Barrragán (1998)), showing an enrichment in oxygen-18, due to rock-water interaction at high temperature, Barragán, Portugal and Arellano (1995), see Figure 2.20.

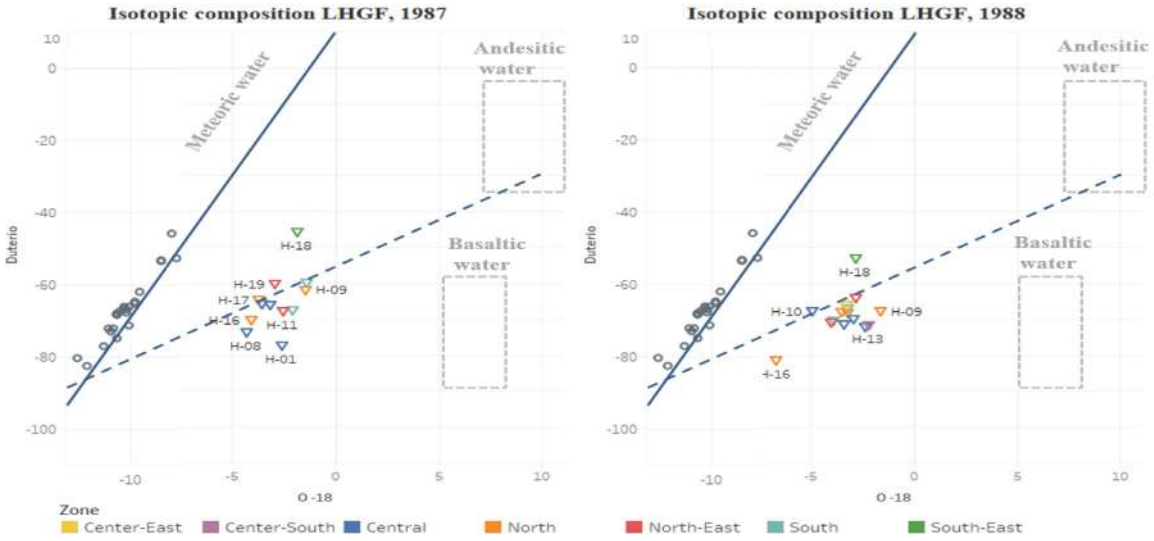

Figure 2.20: Isotopic composition in LHGF. The black circles represent the spring samples in 1996. Data taken from Tovar-Aguado and López-Romero (1999).

Chapter 3

Reservoir Engineering

To start, it is important to differentiate the modeling and simulation concepts. Based on Anu (1997), modeling is the process of producing a model; a model is a representation of the construction and working of some system of interest which should be a close approximation to the real system and incorporate most of its salient features (Model validation techniques include simulating the model under known input conditions and comparing model output with system output). While simulation is a tool to evaluate the performance of a system, existing or proposed, under different configurations of interest and over long periods of real time. In this work, as generally, the reservoir engineering simulation viewpoint is taken from O'Sullivan, Pruess and Lippmann (2001a).

With the advent of digital computers, the numerical solution of complex non-linear partial differential equations became possible in the late 1960s. These techniques have been used to modeling the mass and energy transport in geothermal reservoirs (O'Sullivan et al., 2001a).

3.1 Geothermal Modelling Advances

In early geothermal reservoir simulations the reservoir fluids were idealized as pure water (Program, 1980). Subsequently more realistic representations of geothermal fluids included carbon dioxide, which is usually the most prominent non-condensable gas (Zyvoloski and O'Sullivan, 1980; Pritchett, Rice and Riney, 1981). Later developments include permeability changes from dissolution and precipitation of minerals (Malate and O'Sullivan, 1992; Weir and White, 1996). A fully-coupled treatment of three-dimensional fluid flow and mass transport with detailed chemical interactions between aqueous fluids, gases, and primary mineral assemblages is very difficult. Such treatment can potentially provide a more realistic description of geothermal reservoir processes during natural evolution as well as during exploitation, and can provide added constraints that can help reduce the inherent uncertainty of geothermal reservoir models (O'Sullivan et al., 2001a).

The basic inputs for modeling are as follows

1. A conceptual model of the reservoir
2. Natural state pressure and temperature distribution
3. Well tests and interference tests
4. Production and injection history: mass flow, enthalpy/temperature.
5. Changes in reservoir pressure and temperature during production
6. Well specifications (locations of feed zones)

Other data that can be used are the fluid chemical specifications as well as possible factors that generate subsidence (Grant Malcolm A., 2011).

3.2 Conceptual Model

The conceptual model is the first guide to the numerical model. This incorporates the ideas of the geoscientists working on the reservoir: the construction of a pattern from the mixture of physical information available; surface manifestations (i.e. hot springs, steaming grounds, etc.), flow boundaries, main geologic features such as faults and layers, zones of high and low permeability, isotherms, location of deep inflows and boiling zones, geophysical data (resistivity boundaries, heat flow contours), etc.

Setting up a conceptual model requires the synthesis of information from a multidisciplinary team composed of geologists, geophysicists, geochemists, reservoir engineers and project managers. Some of the raw data require expert interpretation before they can be used. For example, the data sets tend to be incomplete and often the conceptual models proposed by the various contributing scientists and engineers are inconsistent or incorrect. Thus, the "art" of computer modeling involves the synthesis of conflicting opinions, interpretation and extrapolation of data to set up a coherent and sensible conceptual model that can be developed into a computer model (O'Sullivan et al., 2001a).

3.3 Boundary Conditions

Two important matters to be decided in setting up a model of a geothermal system are its size and the boundary conditions to be applied on the sides of the model. Geothermal systems, apart from low-temperature systems, involve the large-scale convection of heat and mass, driven by the deep input of heat. Usually the whole of this convective system is not included in a model, therefore, some those aspects of the convective system must be represented by the boundary conditions. In particular, at the base of the model the deep upflow is represented by a suitable source of heat and mass. The only exception to this procedure is the special case of vapor-dominated

systems, where it is not possible to set up a stable natural state using flow boundary conditions(O'Sullivan, K and Lippmann, 2001b). Instead, constant pressure and vapor saturation boundary conditions must be applied (O'Sullivan, Barnett and Razali, 1990; McGuinness, Blakeley, Pruess and O'Sullivan, 1993).

Constant pressure and temperature boundary conditions instead of flow boundary conditions have been used for modeling hot water or liquid-dominated, two-phase systems. This procedure works satisfactorily but should be used with care as it may lead to a false quasi-steady state in future scenario simulations, where the unlimited recharge from a constant pressure boundary matches the specified production rate. In general the lateral boundaries should be sufficiently remote from the production and injection zones so that the choice of boundary conditions does not significantly affect the performance of the model over the simulated lifetime of the project (O'Sullivan et al., 2001a).

The latter boundary condition allows the free flow of cool water into (or out of) the model. An intermediate approach adopted by some is to apply "recharge" boundary conditions that allow mass flow into (or out of) the boundary blocks at a rate proportional to the pressure drop (or increase). In some instances much more "active" lateral boundary conditions have been applied by specifying mass injection or production at some of the boundary blocks. The problem with this technique is that the flows, and hence the temperature distribution in a natural-state model, can then be matched by adjusting the boundary conditions. The flows are not primarily determined by the permeability structure. Thus, this process makes the external application of the lateral flows or constant pressure and temperature boundary conditions by the modeler the dominant part of model calibration, therefore limiting the utility of the model for predicting future reservoir behavior. In the opinion of the authors, the model should be self-contained as much as possible, with the model structure determining its behavior and not the lateral boundary conditions. If these conditions have a large influence on the behavior of the model it means that the modeled domain is not large enough and the lateral boundaries of the model should be pushed farther out (O'Sullivan et al., 2001a).

In most cases the atmospheric conditions are implemented not at the ground surface but at the estimated position of the water table. Some modelers have used an approximate flat water table at a constant elevation while others have adjusted the thickness of the top blocks of the model to match the variable elevation of the water table (O'Sullivan, Bullivant and Follows, 1998). The difficulty with using a top boundary condition of constant atmospheric conditions is that it may allow the unlimited inflow of cold water or the unlimited outflow of warm fluids. In fact the inflow of cold water cannot exceed the natural infiltration rate. In a real geothermal system, if the shallow pressures fall far enough, the water table will be lowered as well as recharge water being drawn in. There is no easy way of representing this lowering of the water table in a standard geothermal model. The shallow temperature regime, moreover, may not be well represented by a single atmospheric temperature at the water table level. Some have added complexity by estimating the variable temperature at the water table and implementing constant pressure and temperature conditions with a different temperature at each block at the top of the model (O'Sullivan et al.,

2001a).

3.4 Natural State

The first step in model calibration is to match the natural state. The relevant data are the natural temperatures and pressures and the amount of surface discharge of both heat and mass. The permeabilities and the location of the deep upflow are adjusted until a good match is achieved between the results predicted by the model and the data for the downhole temperatures and the locations and strength of the surface features. It is then run until a steady state is reached. Then some parameters, such as permeability and sink/sources, are changed, and the model is rerun until a steady state is obtained that is closer to the observations (Figure 3.1). The process of adjusting parameters to get a natural state match is usually slow. According to O'Sullivan and O'Sullivan (2016) for each step of the calibration process, the model must be is run until a stable steady state is reached, requiring a simulation time of, say, approximately 10^6 years.

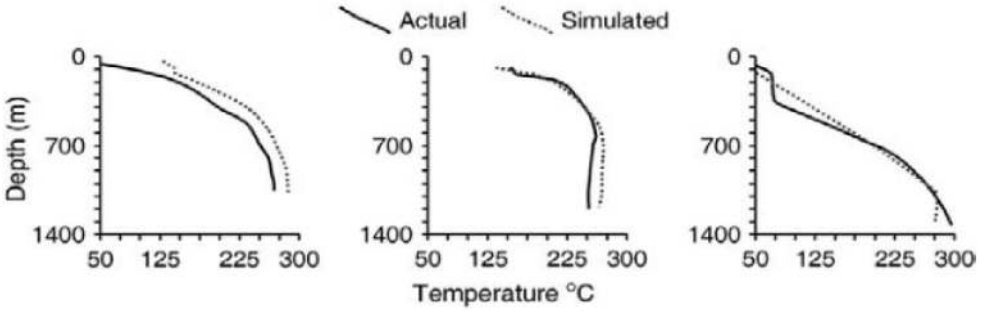

Figure 3.1: Downhole temperature matches. Source: White, 2006. Reproduced with permis- sion of Kawerau Geothermal Ltd., and Ngati Tuwharetoa Geothermal Assets Ltd (Grant Malcolm A., 2011).

3.5 History Matching and Future Scenarios

Once the natural state matching has been achieved, wells are specified, and the model is then used for production runs to simulate the changes under exploitation. This involves adjusting porosities and some local permeability so that the model results match the observed changes over time of production enthalpies and downhole pressures. The parameter changes also affect the natural state model, so it is necessary to rerun the natural state to make sure this match has not been degraded. Further iterations may be needed to get acceptable matches to both the natural state and production history. Figure 3.2 show enthalpy history matches for the Wairakei-Tauhara model of O'Sullivan et al. (2009).

Finally, future scenarios are run to test future production and injection options. It is usual to run future scenario simulations for periods of 25 to 50 years into the

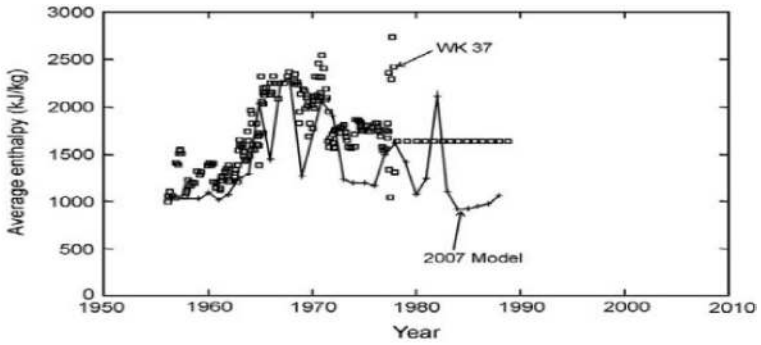

Figure 3.2: History match to WK37 production enthalpy (Grant Malcolm A., 2009).

future. The accuracy of the model predictions is likely to decrease with time, and recently some modelers have been adding uncertainty estimates to their predictions. It is also worthwhile to extend the period for future scenario simulations to check that the long-term behavior of the model is physically credible (O'Sullivan and O'Sullivan, 2016).

3.6 Validation of the Simulation

Ideally a model would be validated by producing a prediction of future field performance and then observing actual behavior and comparing the two. The traditional rule of thumb is that model predictions are valid for roughly the length of time that history has been matched. While there is substantial operating history with some simulations, very little has been published providing such a direct validation. There are three fields for which there are such published "post-audits": Olkaria, Nesjavellir, and Wairakei. In addition, a number of simulations in a range of fields (The Geysers, Cerro Prieto, Mammoth, Heber, Geo East Mesa, Salton Sea, Puna, and Steamboat Springs) are reported to have provided accurate forecasts for periods of 5 to 14 years (Sanyal, 2002).

The main use of computer models has been in estimating the electricity generating potential of undeveloped geothermal fields or for evaluating expansion options for partly developed fields. Also modeling has been extensively used for investigating various production and injection scenarios. Most of the largest and most complex models are too recent to evaluate by comparing their predictions with the actual outcome. Some of these carried out by Bodvarsson, Pruess, Haukwa and Ojiambo (1990) for Olkaria, Kenya. For Olkaria, a set of predictions made in 1987 were evaluated using three additional years of data. The Olkaria East Field is interesting and difficult to model because it contains a vapor-dominated zone underlain by a liquid-dominated region. In the 1987 study, five scenarios were devised for field exploitation involving well spacing, reinjection, and power generation strategies. Thirty-year forecasts of field production were made although it was recognized that predictions were likely to be valid only for as long as the period of the matched history, in this case 6.5 years. In the post-audit (Bodvarsson et al., 1990), a well-by-well comparison was performed,

with the conclusion being that the model adequately predicted steam rates and their decline for about 75% of the wells, with some wells showing unorthodox behavior and some having little history on which to base the calibration. Using a field-wide basis for comparison, the field-wide total decline in steam rate agreed very well with the prediction. The model also predicted the relative contribution of different feed zones to the wells fairly well according to O'Sullivan et al. (2001a).

3.7 Mathematical Theory

Geothermal reservoir models follow laws such as Conservation of Mass, which states that "what goes in must come out", Conservation of heat and Darcy's Law, which determines how hot water and steam move underground.

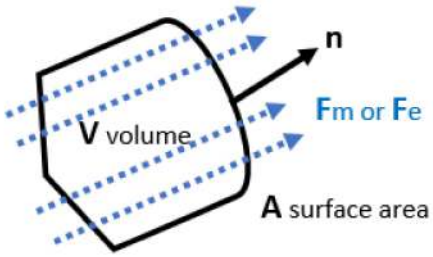

Figure 3.3: Control volume for conservation equations. Fm and Fe is the flux of mass and energy, respectively and n is the normal vector to V. (O'Sullivan et al., 2011)

The first two conservation equations are described by the following equations, considering a control volume shown in the Figure 3.3

$$\frac{d}{dt}\int_V A_m dV = -\int_S n \cdot F_m dA + \int_V q_m dV \tag{3.1}$$

$$\frac{d}{dt}\int_V A_e dV = -\int_S n \cdot F_e dA + \int_V q_e dV \tag{3.2}$$

where:

- A_m, A_e: Is the amount of *mass/volume*, and amount of *energy/volume*
- F_m, F_e: Is the mass and energy flux respectively
- q_m, q_e: Is the amount of mass and energy produced or injected by wells/unit volume respectively

For the general case of two-phase flow, the amount per unit volume of mass is calculated using:

$$A_m = \phi[\rho_l S_l + \rho_v S_v] \tag{3.3}$$

$$A_e = (1-\phi)\rho_r c_r T + \phi(\rho_l u_l S_l + \rho_v u_v S_v) \tag{3.4}$$

where:

- $\rho_r,\ \rho_l$: Are the density of *rock*, and *liquid*, respectively
- $c_r,\ c_l$: Are the specific heat of *rock*, and *liquid* respectively
- $S_l,\ S_v$: Are the *liquid* and *vapour* saturation
- $U_l,\ U_v$: Are the specific internal energies for *liquid* and *vapour*

While the groundwater mass flux is defined by Darcy's law for water and steam as:

$$\text{Total Mass Flux:} \quad F_m = F_{ml} + F_{mv} \tag{3.5}$$

where

$$\text{Water Flux:} \quad F_{ml} = -\frac{kk_{rl}}{v_l}(\nabla P - \rho_l g) \tag{3.6}$$

$$\text{Steam Flux:} \quad F_{mv} = -\frac{kk_{rv}}{v_v}(\nabla P - \rho_v g) \tag{3.7}$$

and for a two-phase flow of water and steam it is given by:

$$\text{Total Energy Flux:} \quad F_e = h_l F_{ml} + h_v F_{mv} - \lambda \nabla T \tag{3.8}$$

where:

- k_l: Is the relative permeability
- P: Pressure
- g: Gravitational acceleration
- h: Enthalpy
- λ: thermal conductivity (of the saturated rock matrix)
- $v_l,\ v_v$: Are the kinematic viscosity of *liquid*, and *vapour* respectively

3.8 Discrete Equations

For numerical simulation it is necessary turn the mass and energy equations into discrete form, dividing the space into blocks or elements and discretizing the simulation time in a sequence of time steps. The TOUGH2 code is based on integrated finite difference method (Edwards, 1972; Narasimhan and Witherspoon, 1976), which avoids any reference to a global system of coordinates, and thus offers the advantage of being applicable to regular or irregular discretizations in one, two, and three dimensions.

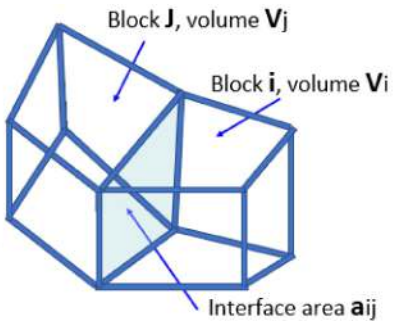

Figure 3.4: Two blocks from a typical TOUGH2 numerical model (O'Sullivan et al., 2011)

For the blocks showed in Figure 3.4 the ith block has volume V_i and is connected by an area of a_{ij} to the jth block. P_i^n and T_i^n are used to represent the pressure and temperature in the ith block at the end of the nth time step. The nth time step is of duration $\triangle t_n$. The procedure discussed here calculates the pressures and temperatures at block centres while fluxes (mass and energy are calculated at block boundaries).

Using the notation above, the discrete mass and energy balance equations (equations 2.1 and 2.2) can be written as follows,

$$V_i(A_{mi}^{n+1} - A_{mi}^n) = -\sum_j a_{ij} F_{mij}^{n+1} \triangle t_{n+1} + Q_{mi}^{n+1} \triangle t_{n+1} \tag{3.9}$$

$$V_i(A_{ei}^{n+1} - A_{ei}^n) = -\sum_j a_{ij} F_{eij}^{n+1} \triangle t_{n+1} + Q_{ei}^{n+1} \triangle t_{n+1} \tag{3.10}$$

where:

- A_{ei}^{n+1}, A_{mi}^{n+1}: Are the amount of mass and energy of fluid per unit volume contained in the ith block at the end of the (n+1)th time step
- F_{mij}^{n+1}, F_{eij}^{n+1}: Are the mass and energy flux from block i to block j evaluated at the end of the $(n+1)th$ time step (calculated using Darcy's law for the flow of fluid through a porous medium)
- Q_{mi}^{n+1}, Q_{ei}^{n+1}: Are the mass and energy production from block i evaluated at the end of the $(n+l)th$ time step

The subscript i refers to the ith computational block while the double subscript ij refers to a quantity evaluated at the interface between block i and block j. The volume of block i is V_i and the area of the ij interface is a ij . The superscript n is the time-step counter, while the size of the current time-step is $\triangle t_{n+1}$.

For the general case of two-phase flow, the amounts per unit volume of mass and energy are discretized as:

$$\text{Mass} \quad A_{ei}^{n+1} = \phi(\rho_l S_l + \rho_v S_v)_i^{n+1} \tag{3.11}$$

$$\text{Energy} \quad A_{ei}^{n+1} = (1-\phi)\rho_{ri}c_{ri}T_i^{n+1} + \phi_i(\rho_l u_l S_l + \rho_v u_v S_v)_i^{n+1} \tag{3.12}$$

Steam table data are supplied through an equation of state module (EOS) to calculate the secondary parameters, $\rho_l,\ \rho_v,\ u_l,\ u_v,\ v_l,\ v_v$, and the primary variables are P and T (and S_v for two-phase conditions).

The discrete version of Darcy's law is given by:

$$\text{Water} \quad F_{ml,ij}^{n+1} = -(\frac{kk_{rl}}{V_l})_{ij}^{n+1}[\frac{P_j^{n+1} - P_i^{n+1}}{d_{ij}} - \rho_{l,ij}^{n+1} g_{ij}] \tag{3.13}$$

$$\text{Steam} \quad F_{mv,ij}^{n+1} = -(\frac{kk_{rv}}{V_v})_{ij}^{n+1}[\frac{P_j^{n+1} - P_i^{n+1}}{d_{ij}} - \rho_{v,ij}^{n+1} g_{ij}] \tag{3.14}$$

where d_{ij} is the distance between block centers.

Total mass flow (eq. 2.5) is given by

$$F_{m,ij}^{n+1} = F_{ml,ij}^{n+1} + F_{mv,ij}^{n+1} \tag{3.15}$$

Total energy flow (eq. 2.8) is given by

$$F_{e,ij}^{n+1} = h_{l,ij}^{n+1} F_{ml,ij}^{n+1} + h_{v,ij}^{n+1} F_{mv,ij}^{n+1} - \lambda_{ij}^{n+1}[\frac{T_j^{n+1} - T_i^{n+1}}{d_{ij}}] \tag{3.16}$$

The key to a successful numerical scheme is the way the interface quantities are evaluated. A straightforward average is applied to calculating the densities in the gravity term, and a harmonic mean is usually used for calculating the rock permeability k_ij . However, for the relative permeabilities and kinematic viscosities, upstream weighting must be used. In Eq. 3.16, harmonic weighting is used to calculate the thermal conductivity at the interface, whereas upstream weighting is used for evaluating enthalpies (O'Sullivan and O'Sullivan, 2016). The first two terms on the right side of this equation correspond to convective energy transport, i.e. mass transport carrying energy. The final term represents conductive energy transport resulting from temperature gradients).

Upstream weighting of interface quantities ($k_{rl},\ k_{rv},\ h_l,\ h_v,\ v_l,\ v_v$) e.g.

$$\text{Flow from block } j \text{ to } i \quad (\frac{k_{rl}}{v_l})_{ji}^{n+1} = (\frac{k_{rl}}{v_l})_j^{n+1} \tag{3.17}$$

$$\text{Flow from block } i \text{ to } j \quad (\frac{k_{rl}}{v_l})_{ij}^{n+1} = (\frac{k_{rl}}{v_l})_i^{n+1} \tag{3.18}$$

The implicit Euler method for time-stepping and upstream weighting of mobilities (ie, relative permeability divided by kinematic viscosity) and enthalpies have both been implemented in well-known geothermal simulation codes with two-phase capability, such as TOUGH2, TETRAD, FEHM, and STAR (O'Sullivan and O'Sullivan, 2016).

3.9 TOUGH2 Simulator

TOUGH2 is a general-purpose numerical simulation program which solves mass and energy balance equations that describe fluid and heat flow in general multiphase, multicomponent systems (Section 3.7). Fluid advection is described with a multiphase extension of Darcy's law; in addition there is diffusive mass transport in all phases. Heat flow occurs by conduction and convection, the latter including sensible as well as latent heat effects. The description of thermodynamic conditions is based on the assumption of local equilibrium of all phases. The original TOUGH2 code released in 1991 (Pruess, 1991a) provided five different fluid property or "EOS" (equation-of-state) modules (Figure 3.5). The new TOUGH2 version 2.0 includes improved versions of these five EOS-modules and 4 more, but this work are focused on simulations using EOS3 (water, air, multi-phase).

Module	***Capabilities***
EOS1	water, water with tracer
EOS2	water, CO2
EOS3	water, air
EOS4	water, air, with vapor pressure lowering
EOS5	water, hydrogen

Figure 3.5: TOUGH2 fluid property modules, Pruess et al. (1999).

3.9.1 Methodology and Architecture of TOUGH2

Scope and methodology

The discretization results in a set of strongly coupled nonlinear algebraic equations (Section 3.7), with the time-dependent primary thermodynamic variables of all grid blocks as unknowns, solved simultaneously, using Newton-Raphson iteration. Time steps can be automatically adjusted (increased or reduced) during a simulation run, depending on the convergence rate of the iteration process. Automatic time step adjustment is essential for an efficient solution of multiphase flow problems.

Program Structure and Execution

The governing equations for multiphase fluid and heat flow (Section 3.7) have the same mathematical form, regardless of the nature and number of fluid phases and components present. Based on this recognition, TOUGH2 (Transport Of Unsaturated Groundwater and Heat) was set up with a modular architecture (see Figure 3.6), in which the main flow and transport module can interface with different fluid property modules. This gives TOUGH2 the flexibility to handle a wide variety of multicomponent, multiphase flow systems. The nature and properties of specific fluid mixtures enter into the governing equations only through thermophysical parameters,

such as fluid density, viscosity, enthalpy, etc., which are provided by an appropriate "EOS" (equation-of-state) module. Such an architecture was first implemented in a research code known as MULKOM in the early 80s, and later formed the basis of TOUGH, a more specialized multiphase code for water-air-heat (Pruess, 1987).

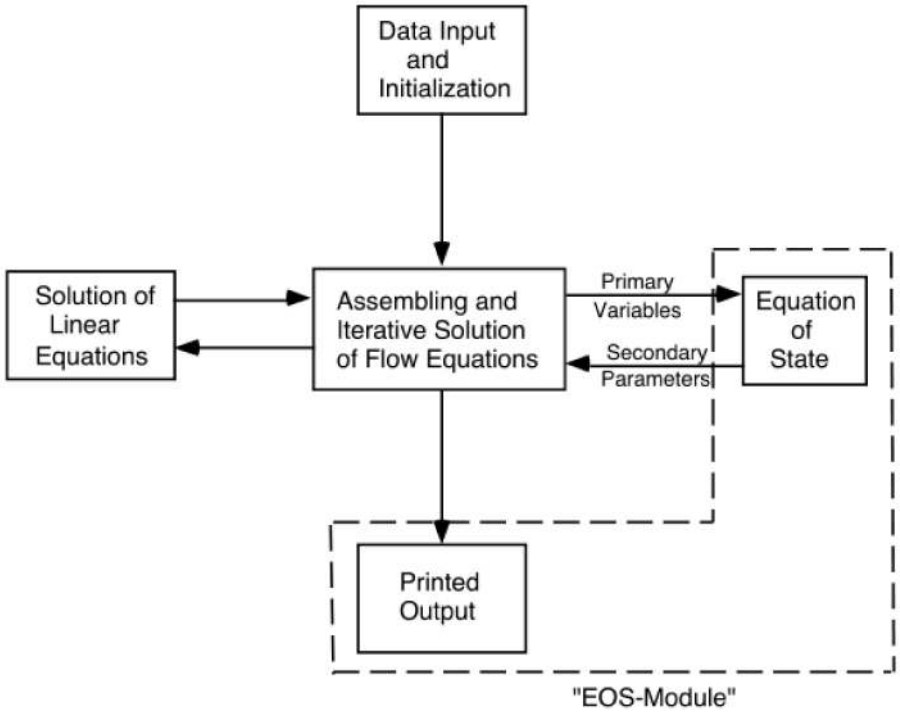

Figure 3.6: Modular "MULKOM" architecture of TOUGH2 (Pruess et al., 1999).

TOUGH2 Array Structure

It is suggested to see Pruess et al. (1999) that provide details on TOUGH2 structures the primary thermodynamic variables and secondary parameters (thermophysical properties; Saturation, relative permeability, viscosity, density, specific enthalpy, capillary pressure and diffusion factors). The number of phases determines the number of the balance equations per grid block (as this work use two phases will be three equations per block). Finally the TOUGH2 Manual discusses how these equations are solved through Newton-Raphson method to get the values of the primary thermodynamic variables for the next time step.

3.9.2 Equation-of-State Modules

The thermophysical properties of fluid mixtures needed for assembling the governing mass and energy-balance equations are provided by "equation-of-state" (EOS) modules. Fluid phase conditions are recognized from the numerical values of the primary variables. Besides providing values for all secondary (thermophysical) parameters as functions of the primary thermodynamic variables, the EOS module fulfills three

additional important functions: (i) the phase conditions pertaining to a given set of primary variables are identified for all volume elements (grid blocks); (ii) the appearance or disappearance of phases is recognized by changes in primary variables change during the Newton-Raphson iteration process; (iii) primary variables are switched and properly re-initialized in response to a change of phase.

EOS1 (water, water with tracer)

This is the most basic EOS module, providing a description of pure water in its liquid, vapor, and two-phase states. All water properties (density, specific enthalpy, viscosity, saturated vapor pressure) are calculated from the steam table equations as given by the International-Formulation-Committee (1967). The formulation includes subregion 1 (subcooled water below T = 350 °C), subregion 2 (superheated steam), and subregion 6 (saturation line up to T = 350 °C). In these regions, density and internal energy are represented within experimental accuracy. Vapor pressure lowering from capillary and adsorption effects are neglected; thus, in two-phase conditions vapor pressure is equal to saturated vapor pressure of bulk liquid. The primary variables for a single-phase conditions are P, T, [X] (pressure, temperature, (mass fraction of water)). For two-phase conditions the primary variables are Pg , Sg , [X] (gas phase pressure, gas saturation, (mass fraction of water)).

EOS3 (water, air)

EOS3 is an adaptation of the EOS1, and implements the same thermophysical properties model (Pruess, 1987). Air is approximated as an ideal gas, and additivity is assumed for air and vapor partial pressures in the gas phase, Pg = Pa + P v . The viscosity of air-vapor mixtures is computed from a formulation given by Hirschfelder et al. (1954). EOS3 differs from the EOS1 in choice of primary thermodynamic variables. The choice made in EOS3 of TOUGH2 is (P, X, T) for single-phase, (Pg , Sg + 10, T). The rationale for the seemingly bizarre choice of Sg + 10 as a primary variable is as follows. As an option, we wish to be able to run isothermal two-phase flow problems with the specification NEQ (is the number of equations, mass and heat balances) = NK (Number of mass components), so that the then superfluous heat balance equation needs not be engaged. This requires that temperature T be the third primary variable. The logical choice of primary variables would then appear to be (P, X, T) for single-phase and (Pg , Sg , T) for two-phase conditions. Taking the second primary variable for two-phase conditions to be X2 = 10+Sg , the range of that variable is shifted to the interval (10, 11), and a distinction between single and two-phase conditions can be easily made.

Chapter 4

Conceptual and Numerical Models

This chapter discusses how the conceptual model was designed, its structures, geological units and main directions of flow. It also discusses how the conceptual model was used to develop the numerical model used to carry out the numerical simulations in AUTOUGH.

4.1 Conceptual Model

The construction of LGHF 3D conceptual model (Figure 4.2) was mainly based on well data published by CFE (see Section 2.2). The data and hydrological schemes were digitized and input into the LeapFrog software. Information such as the 3D temperature distribution (Figure 4.1a) and wairakite, biotite and garnet thresholds (Figure 2.14) were included to design the geothermal reservoir, heat sources and magmatic intrusive (Figure 4.1b. intercepted by H-09 and H-11 at north and H-12 at the south zone). The groundwater flow was based on a 2D interpolation of the water table levels (Figure 2.13)

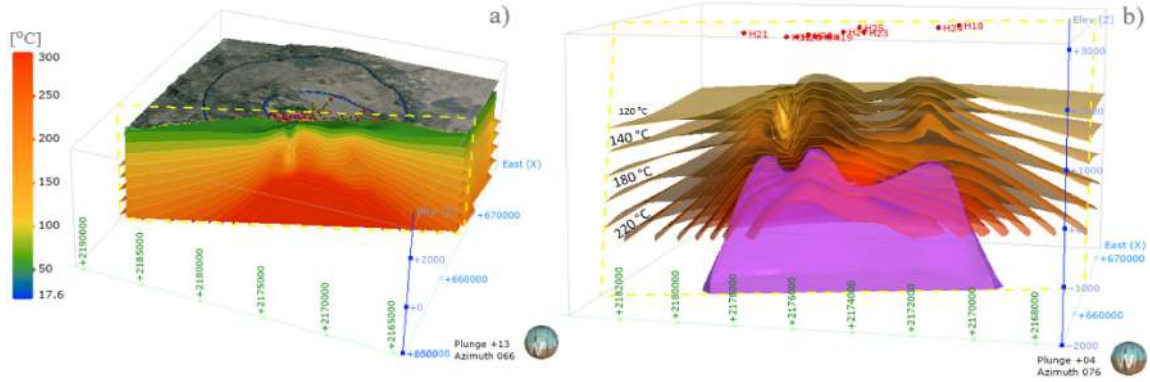

Figure 4.1: a) 3D temperature field interpolated with the CFE temperature logs (Torres-Rodríguez, 1992; Izquierdo-Montalvo et al., 2008; Díaz, 2018). b) A zoom to the magmatic intrusive and some isotherms to analyze the positive correlation between the highest temperature zones and the shallowest occurrences of the magmatic intrusive.

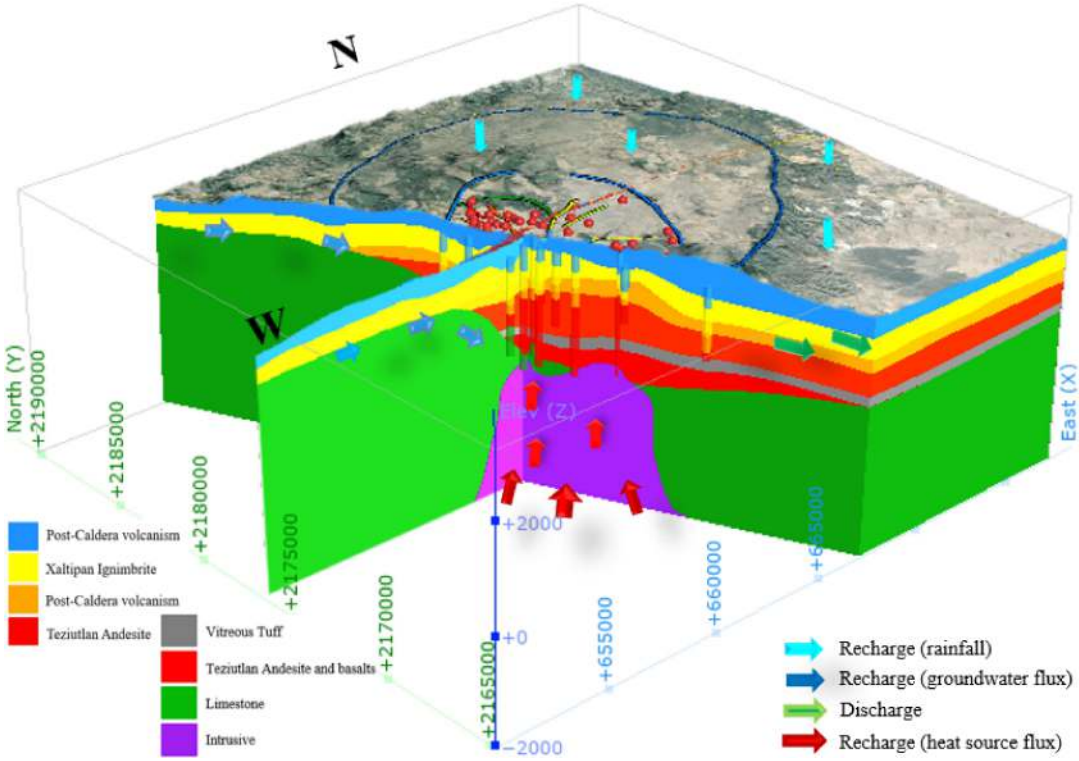

Figure 4.2: 3D model of LHGF whose base reaches 2000m below sea level, this includes the magmatic intrusive. The basement increases in width in the N-W direction. The red geological units are mainly the Teziutlán Andesite and correspond to the geothermal reservoirs. The arrows show the flow pattern in LHGF and the cylinders represent the wells showing the different geological units reached.

4.2 Numerical Models

To carry out the discretization of the conceptual model a mesh was made with an octagonal shape. This allows the lateral recharge and discharge surfaces to be at a radius of 9000m from the production zone (Figure 4.3b) and should avoid a direct influence of the boundary conditions. The internal design of the mesh was of Voronoi type, but in the current production area, the mesh was set up with a higher spatial resolution in order to place each well in different column, as well as to achieve a good representation of the geological structures. The mesh was oriented in the direction of the main superficial thermal manifestations (the most permeable faults direction NE-SE, Figure 4.3a). The vertical structure ranges from topographic levels down to 2000 meters below sea level with a logarithmic design, increasing spatial resolution in the water table range (2200 to 2800 m.a.s.l., Figure 4.3c and 4.3d).

The geological units were discretized as shown in Figure 4.4, Figure 4.5 shows some isotherms to demonstrate the positive correlation between the highest temperature and the shallowest magmatic intrusive occurrences. In these figures the limestone basement configuration can be appreciated by noticing that the width increases in the NW direction, which apparently produces a lower reservoir with a smaller thickness

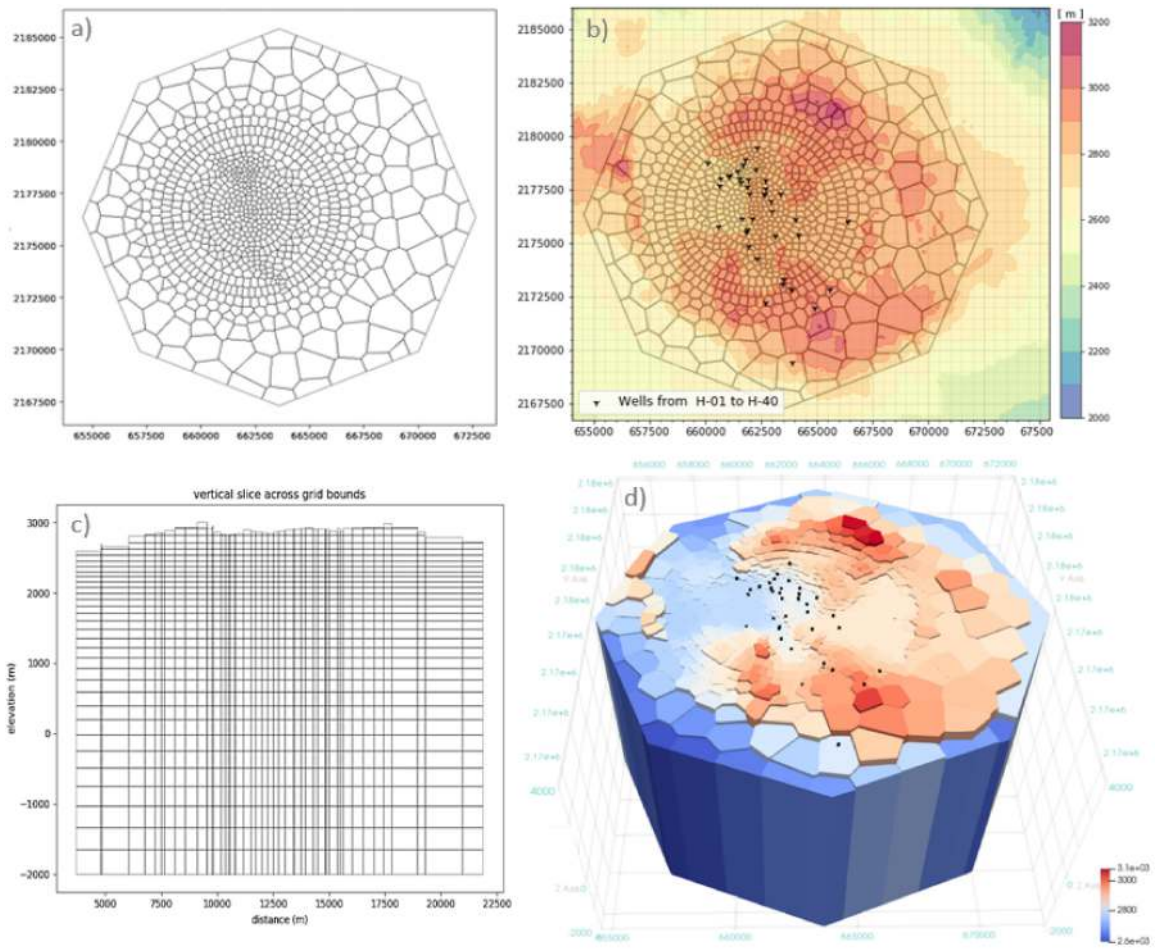

Figure 4.3: Mesh designed to discretize the 3D geological model (Figure 4.2). The mesh has a voronoi design, and more resolution in the production of LHGF, which covers the area showed in Fgire b), with 37 layers reaching -2000m (Figure c), comprising a total of 32,013 blocks. While the Figure d) shows the discretization of the topography. The wells of LHGF are in black color.

in that direction. In addition, the geological structures and faults were discretized (Figure 4.6b). The lowest permeability was assigned to "Los Humeros Caldera", "Las Papas Fault" and structures which delimit the reservoir and act as hydrological barriers; "Los Potreros Caldera", "La Antigua F.", "Mastaloya F.", "Las Viboras F." and the "Main Collapse". The highest permeability was assigned to the faults which controls the superficial thermal manifestations such as "Los Humeros F.", "La Cuesta F.", "Loma Blanca" and "Los Conejos F." (Figure 2.11).

Furthermore, the basement and the upper reservoir were split into three and two layers respectively, since at different depths these are subject to different pressure and temperature, among other factors that modify their petrophysical properties. Not only were these units modified, but also a new type of rock was also added for each geological stratum intersected by a particular fault, summing up to a total of 137 rock types (Figure 4.6a).

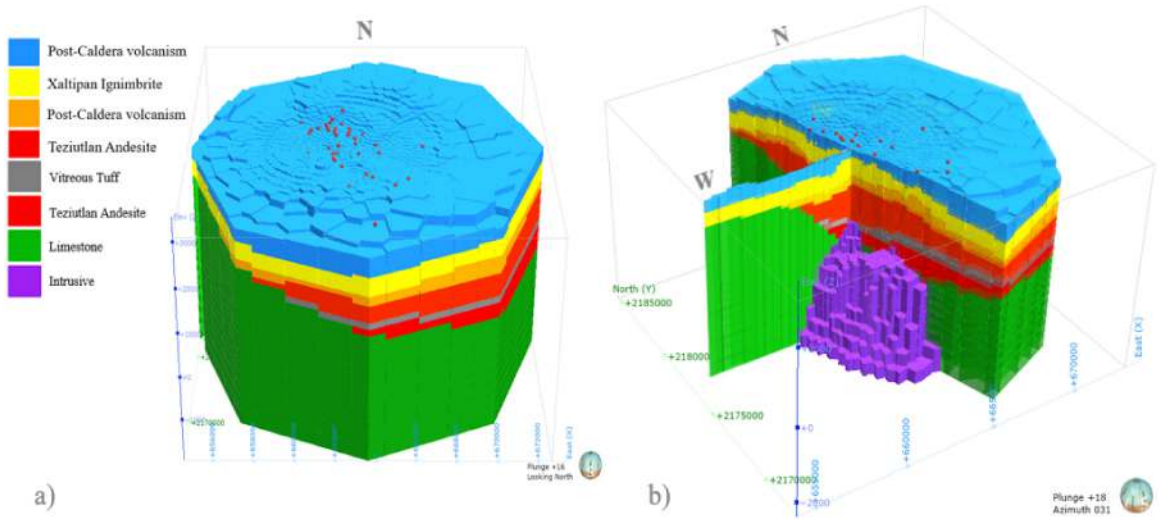

Figure 4.4: 3D geological discretized model, from LHGF conceptual model (Figure 4.2) with a Voronoi mesh (Figure 4.3).

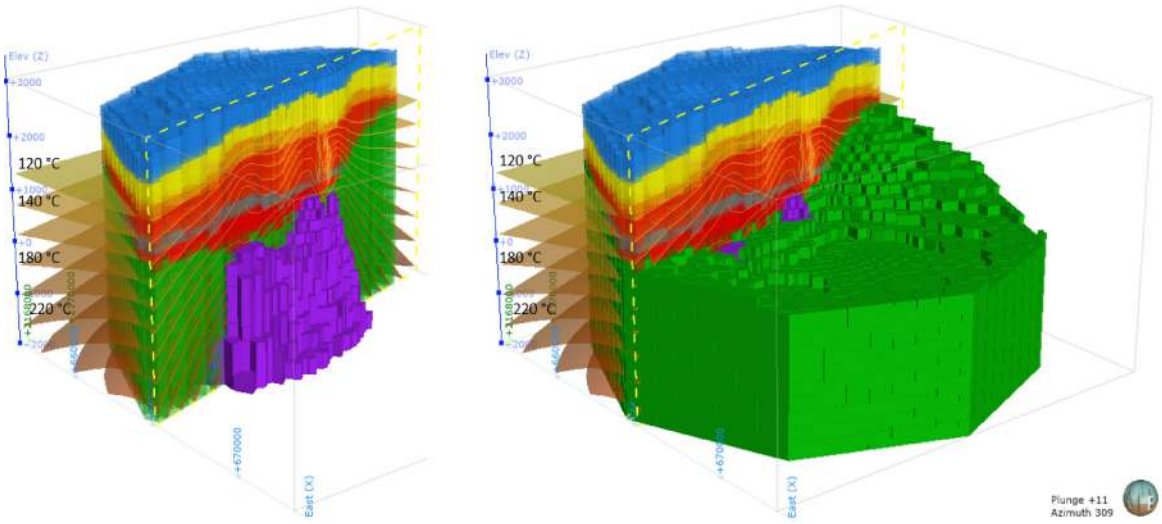

Figure 4.5: Slides of the discretized model which shows the basement structure and the relationship between the highest temperature zones and the intrusive occurrences.

4.2.1 Boundary Conditions

The boundary conditions were set up with PyTOUGH, similar to the assignment of petrophysical properties. The boundary conditions were Dirichlet type, due the good results obtained in different simulations (O'Sullivan et al., 2001a). These models have proved to be useful even for up to 25 years after the calibration date (in this case 25 years after 2012), in addition, the simulation time is much lower compared with a simulation using variable boundary conditions. The boundary conditions include a meteoric recharge of 827mm (annual rate in Los Humeros), at a temperature of $17°C$ and an infiltration rate of 10%. The discharge (at N and S, S-E edges) and recharge (at W and E edges) were set up with a flow 100 times larger than the rainfall rate

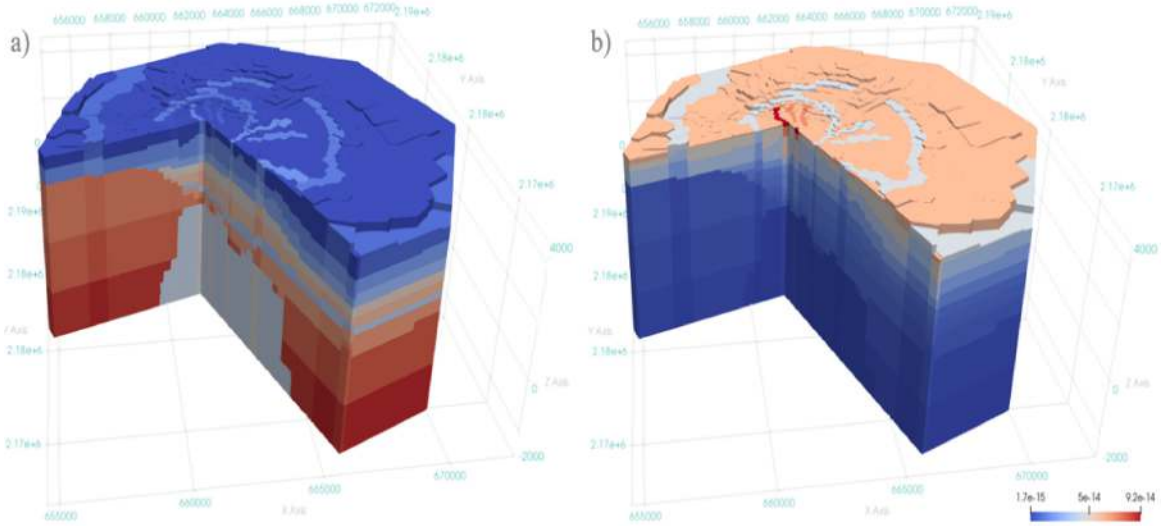

Figure 4.6: Model which shows the 137 rock types. b) Model showing the different permeabilities assigned (1.7e-15 to 9e-14 m2) to each rock type by a different color.

flow but in a lateral area 100 times smaller. The discharge elevation was set at 100m above water table levels (2200-2800m.a.s.l.), while the recharge was set at 300m below the water table levels. An input of very hot water was assigned at the bottom of the model, based on the 3D temperature distribution.

Chapter 5

Calibration of the Natural State Model

The first simulations were performed with a stratified model (Figure 5.1c). Consistent results were obtained in the direction of the mass flow (mainly NE) but the temperature distribution was incorrect in the areas adjacent to the reservoir (Figures 5.1a and 5.1b). This error can be clearly seen when comparing the results with the temperature logs (Figure 5.2) of wells H-27 and H-23 which are outside the area of interest.

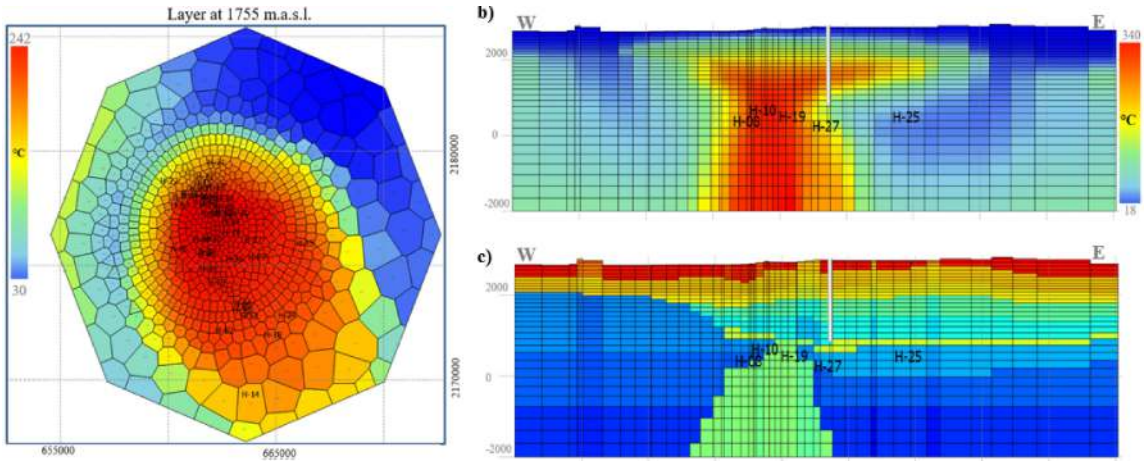

Figure 5.1: Temperature distribution in layer 16, obtained from a numerical simulation using a stratified model. b) Lateral temperature distribution, obtained on an E-W slice. c) Geological units configuration (TIM, University of Auckland Software).

New geological units were created to laterally delimit the areas where the geothermal reservoirs are hosted (area enclosed by "Main Collapse", "Los Humeros F.", "" La Antigua", ""Mastaloya" and "Las Viboras" faults, shown in 5.3). This amended model showed a noticeable improvement in the temperature distribution (Figure 5.4a,b). It contained a total of 143 types of rocks (Figure 5.3), whose permeabilities ranged from 1.5e-15 m^2 to 1.0e-12 m^2, but in the geothermal reservoir area the permeability was established in a range of 1e-15 m^2 to 3e-15 m^2 in X and Y directions

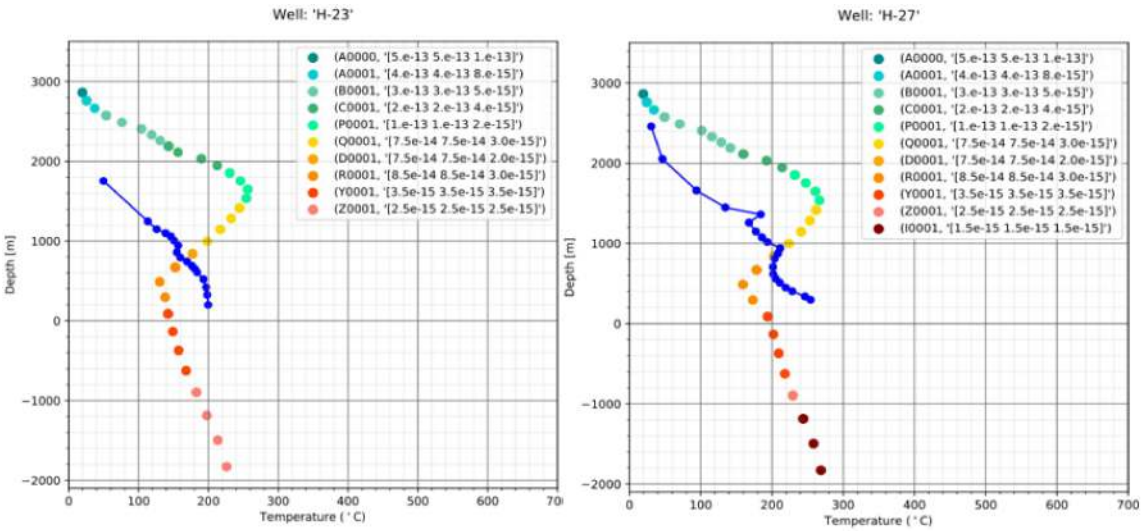

Figure 5.2: H-23 and H-27 temperature logs for the temperature distribution shown in Figure 5.1. Each color represents a different geological unit in the model. And the blue points represent the temperature registered.

while the permeability in the Z direction ranged from 1e-15 m^2 to 8e-15 m^2.

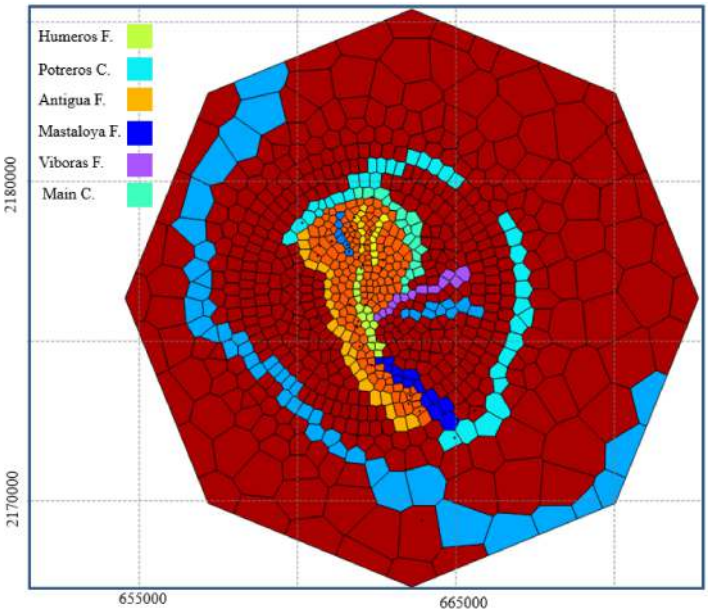

Figure 5.3: Top surface of numerical model. The orange zone represents how the model was laterally modified to delimit the geothermal reservoir zone (orange area), and the names shown are the faults which delimit the reservoir. This model has a total of 143 rock types.

After hundreds of numerical simulations, adding new types of rocks, adding more depth to the model and changing petrophysical properties (mainly permeabilities) in order to get the closest match of model temperatures to the well logs and while maintaining the correct water table levels, the temperature profiles shown in Figures

A1 to A4 were finally obtained. These display the results in different areas of the geothermal field; North, Center, South and areas outside the reservoir. The results outside the reservoir (Figure A3) still show an error in the temperature distribution below layers 12 and 13. Many modifications in petrophysical parameters were tried, but the only way to correct the temperature was by considerably reducing the flow to the discharge zones, but this modification produced incorrect water table levels. Therefore it was decided keep the good match to the water table levels (Figure 5.5) and accept some mismatch with the temperature logs outside the reservoir.

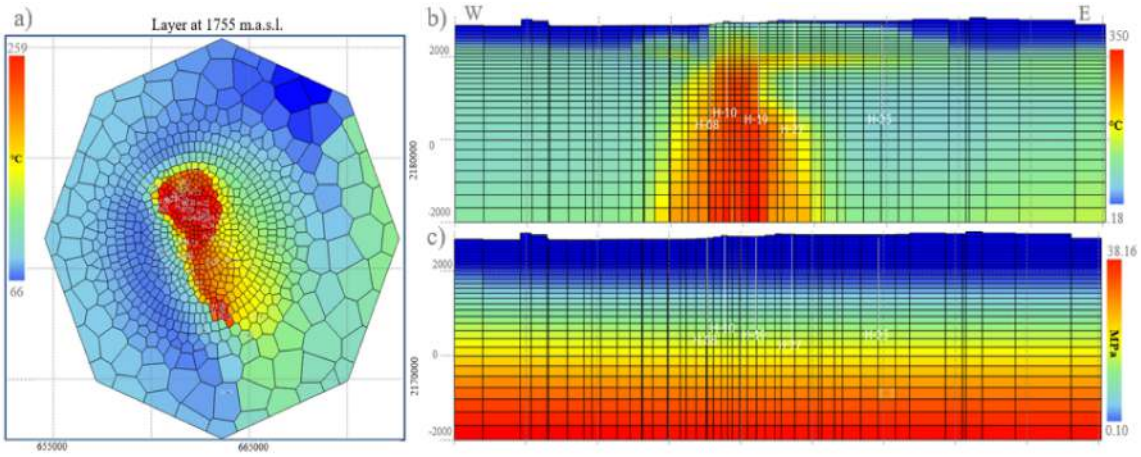

Figure 5.4: a) Temperature distribution in layer 16, obtained from the last numerical simulation using the model shown in Figure 14. b) Lateral temperature distribution, obtained on an E-W slice. c) Pressure distribution showing a direct relationship between the low-pressure zones and high gas saturation zones (see Figure 5.5).

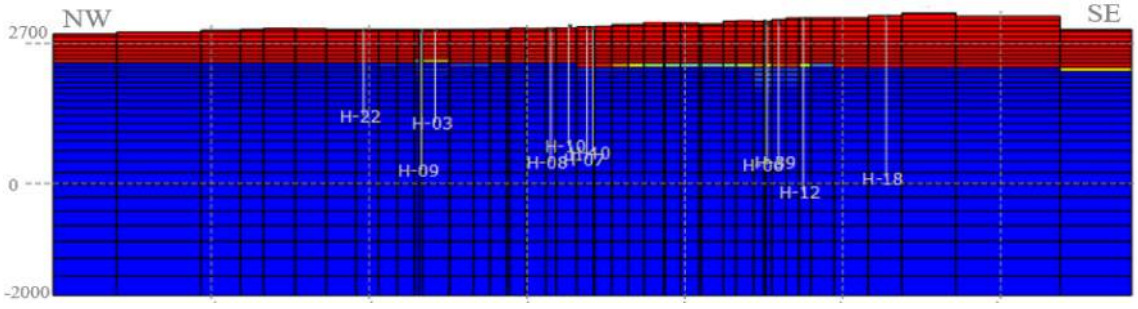

Figure 5.5: Gas saturation distribution in NW-SE direction, which corresponds to the water table shown in Figure 3. The red color corresponds to gas saturation of 0.99 and blue to 0.

Finally, a vector field showing the mass and heat flows was generated (Figure 5.6), to demonstrate the consistency of the results for the mass flow (direction of the recharge and discharge vectors) and the temperature distribution (size of the vector) of the natural state model compared to the conceptual model (Figure 4.2).

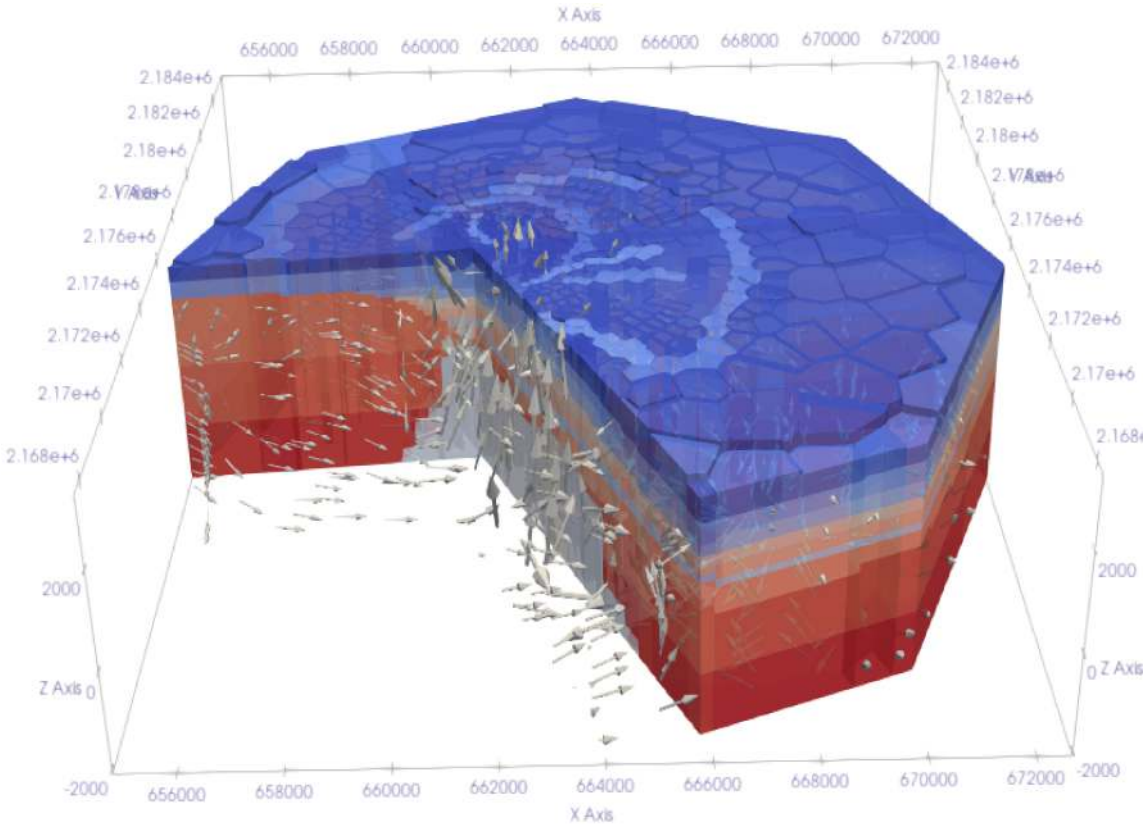

Figure 5.6: Geological model and the vector field of the heat flow with the temperature as scalar used to modify the size of the vectors. It is clearly shows how the natural state correctly represents the groundwater pattern if it is compared with the conceptual model shown in Figure 4.2 and based on the range of water table levels (Figure 5.5).

Chapter 6

Conclusions

Using an algorithm that solves the inverse problem (such as iTOUGH2) and automatically calibrates the model, would have shortened the simulation time, although the experience of making all the modifications manually provides a deeper understanding of how the simulator works and it is possible to make more creative modifications, such as adding new rock types laterally to the model. On the other hand, based on temperature logs and water table levels the LHGF natural state model produces a good match to the data, thus demonstrating that this model is ready to be used to set up a production history model and also models for simulating proposed future production scenarios. But due to the high enthalpies reached in the field, for future simulations it is suggested to use a supercritical EOS.

Identifying the thresholds of the autogenetic minerals and the identification of the different temperature patterns in the field were essential steps in delimiting the geothermal reservoir and for establishing a good conceptual model. Furthermore, these temperature patterns were essential for carrying out a more detailed subdivision of the geological units. The calibration of the model, inside and outside the area of the geothermal reservoir, was improved by the lateral division of the geological units. Besides matching the temperature profiles, a good match to water table levels was obtained, with reasonable outflow rates but with low permeabilities in the upper layers. Although the shallow gas saturation distribution is consistent with the water table data it is necessary to have a higher density of the water table data in areas adjacent to LHGF, in order to obtain a better calibration of the shallow hydrology. This improvement and records of pressure will help to achieve a better calibration of the model and would help in planning the location of future production and injection wells.

Finally, thanks to the annual growth analysis of economic investment and energy production, it was possible to show the important role of geothermal energy throughout history. In addition to its constant growth in energy production, it has proven to be more profitable than other renewable energies. Fortunately, Mexico has extensive and accessible geothermal resources, so it is undoubtedly suggested to continue investment and development in this energy sector.

Appendix A

This appendix shows the results obtained for the numerical model calibrated and generated with AUTOUGH2, for each of the wells available in LHGF. The figures are classified according to certain zone of the LHGF (North, South, Central and the area outside the main reservoirs).

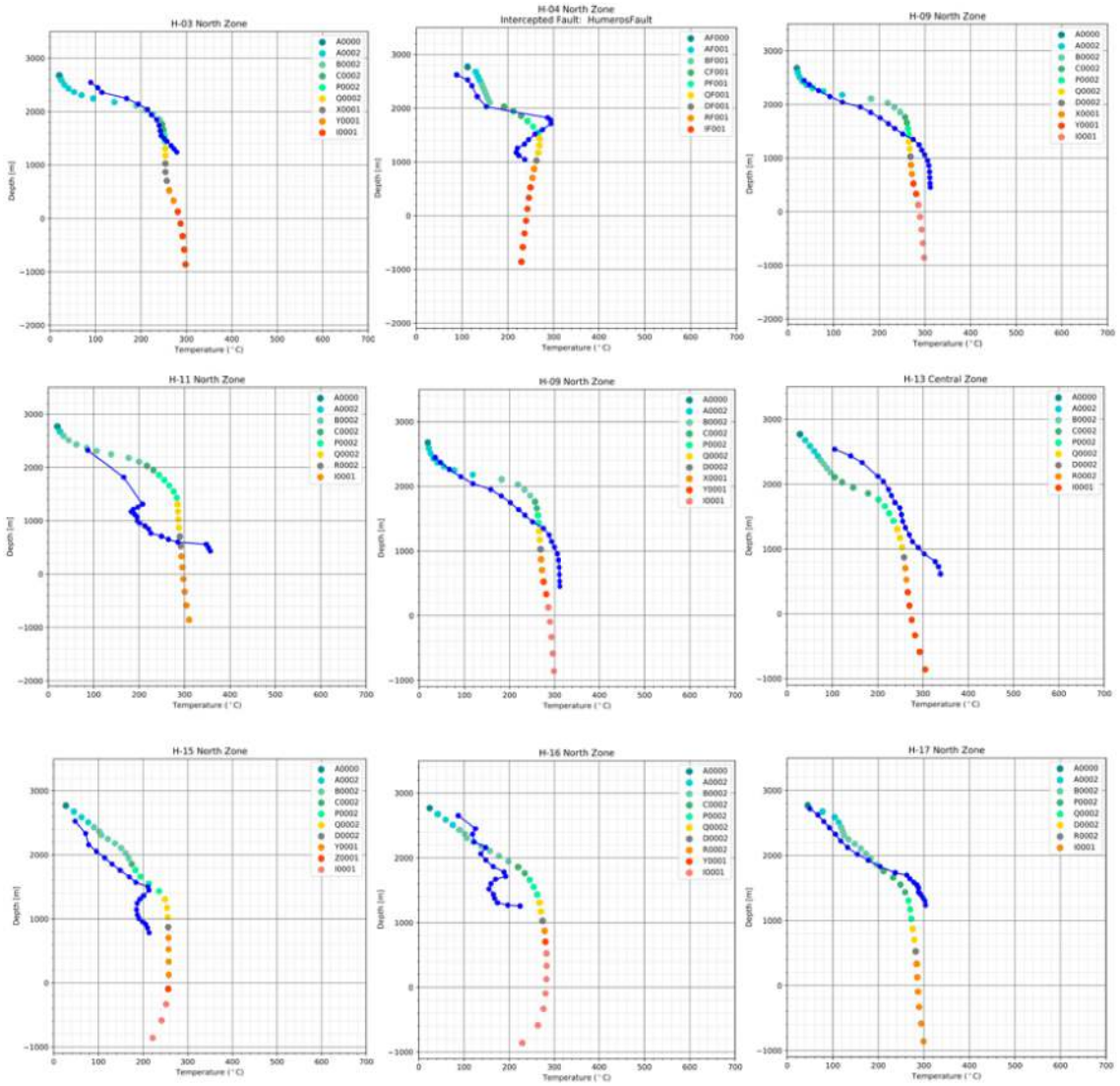

Figure 1: Temperature logs and temperatures resulting from the last simulation for the North zone. Each color represents a different geological unit (see Figure 4.6).

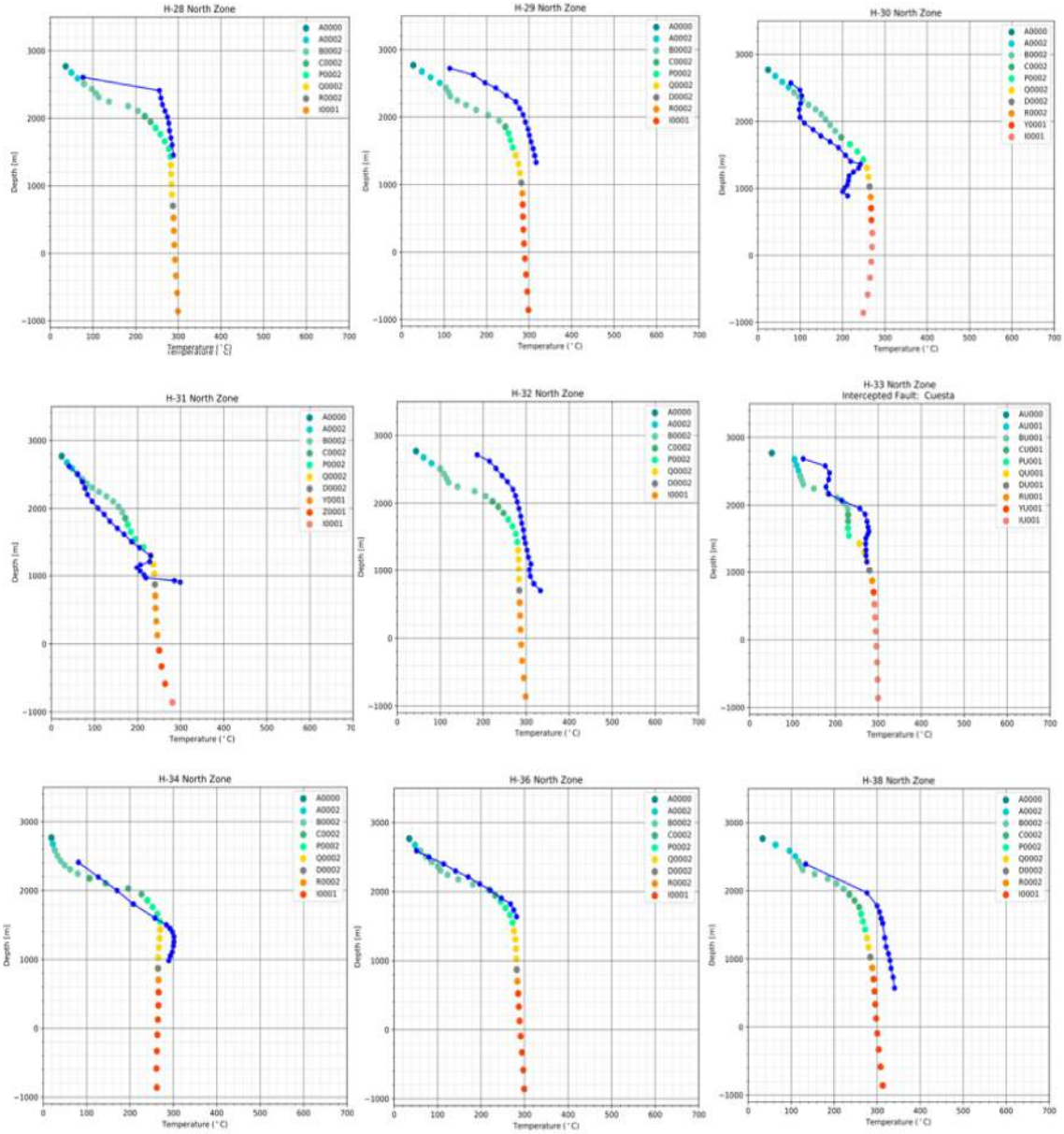

Figure 2: Temperature logs and temperatures resulting from the last simulation in the North zone.

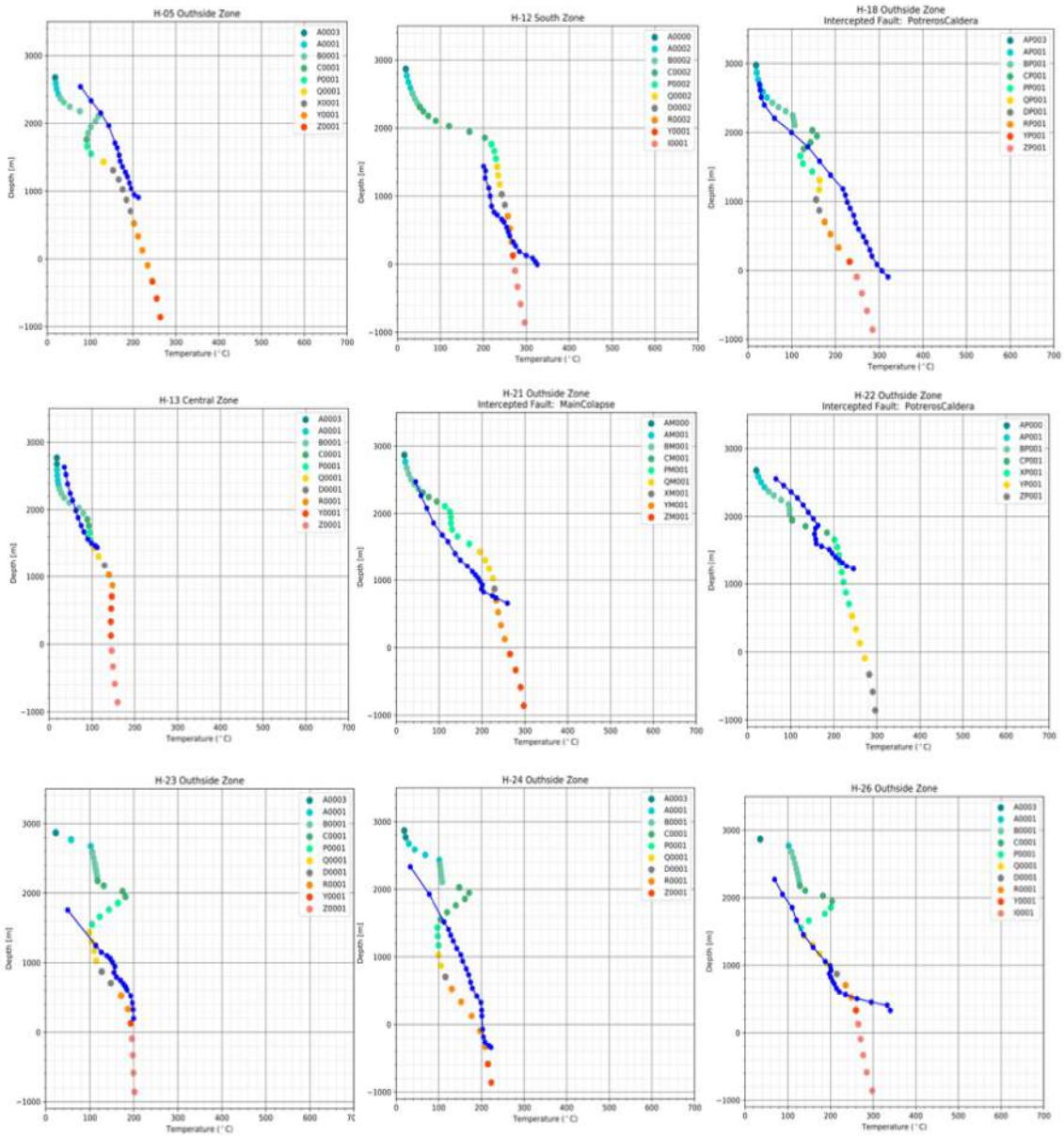

Figure 3: Temperature logs and temperatures resulting from the last simulation for the area outside the reservoir.

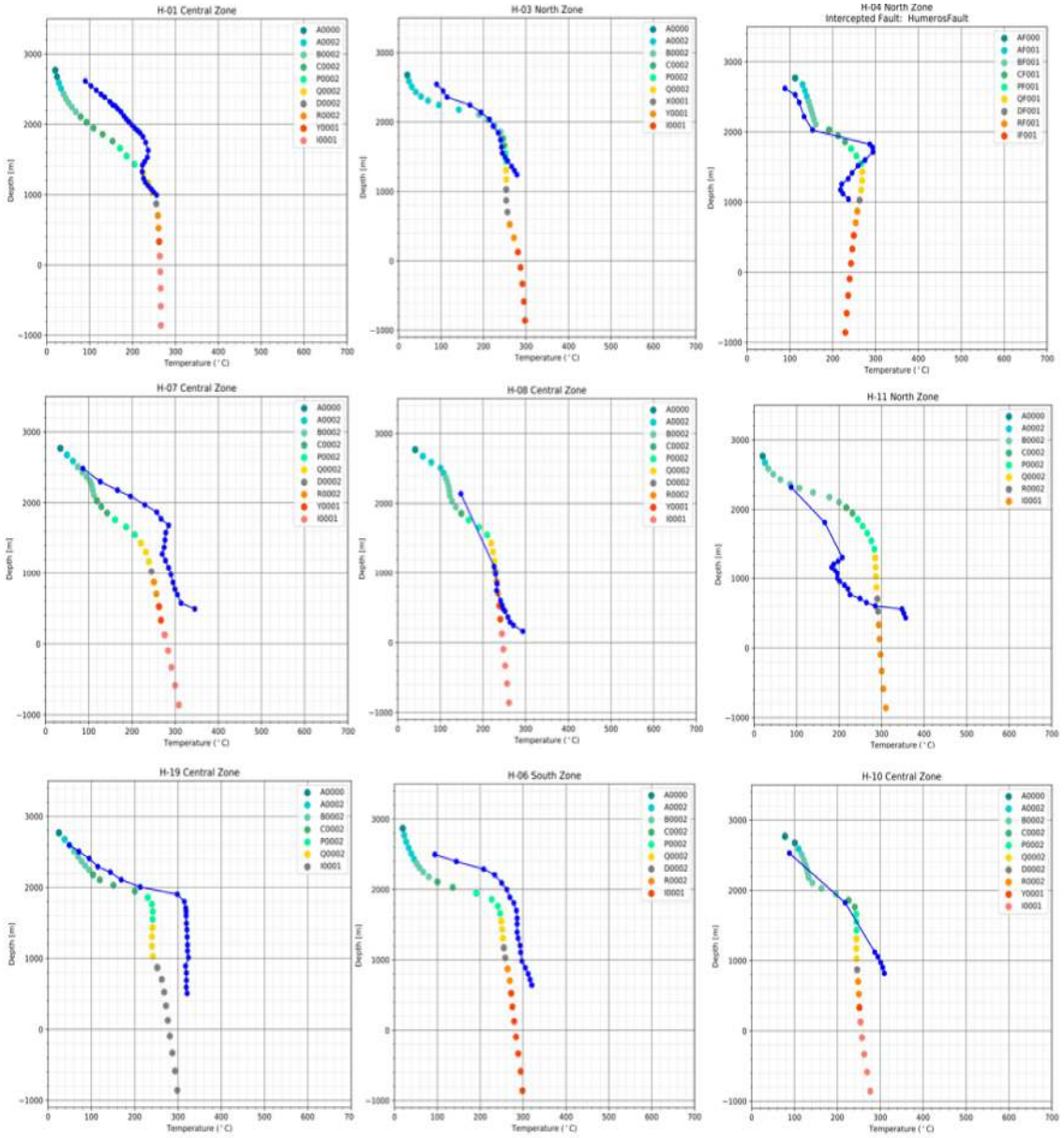

Figure 4: Temperature logs and temperatures resulting from the last simulation for the Central and South zone.

Bibliography

Anu, M., 1997. Introduction to modeling and simulation. Winter Simulation Conference , 7–13.

Arellano, G., García, G., Barrragán, R., 1998. Desarrollo de un modelo básico actualizado del yacimiento de los humeros, puebla. Informe técnico para la comisión Federal de Electricidad 1, 450p.

Arellano, V., Barragán, R., Ramírez, M., 2015. The response to exploitation of the los humeros (méxico) geothermal reservoir. Proceedings World Geothermal Congres , 1–7.

Barragán, R., Portugal, Arellano, V., 1995. Evolución isotópica(1987-1994) de fluidos de pozos del campo geotérmico los humeros, puebla, méxico. Actas INAGEQ 1, 227–231.

Barragán, R., Santoyo, G., Nieva, G., 1989. Caracterización del fenómeno de corrosión-obstrucción de los pozos de los humeros. Informe técnico para la comisión Federal de Electricidad 11, 1–83.

Bodvarsson, G., Pruess, K., Haukwa, C., Ojiambo, S., 1990. Evaluation of reservoir model predictions for olkaria east geothermal field, kenya. Geothermics 19, 399–414.

Carrasco-Núñez, G., Hernández, J., De-León, L., 2017. Geologic map of los humeros volcanic complex and geothermal field, eastern trans-mexican volcanic belt. Journal of Volcanology and Geothermal Research 1, 1–11.

Castillo-Hernández, D., 1999. Determinación geológica de los límites, área y volumen del yacimiento geotérmico de los humeros, puebla, méxico. Rev. Mex. de Geoenergía 15, 69–76.

CONAGUA, 2016. Relación de acuíferos con red piezométrica. registro de datos piezométricos por pozo de observación. mapa que muestra la ubicación de las redes y pozos piezométricos. hidrógrafos de pozos de conagua. URL: https://datos.gob.mx/busca/dataset/red-piezometrica-mapas.

Croucher, A., 2018. PyTOUGH user's guide. University of Auckland Auckland, New Zealand.

De la Cruz, V., 1983. Estudio geológico a detalle de la zona geotérmica los humeros, pue. International Report , 51.

Díaz, Martos, A.S., 2018. Steady state numerical modelling of los humeros goethermal field (master's thesis). Iceland School of Energy. (Thesis of 30 ECTS credits) .

Edwards, A., 1972. State temperature distributions in multidimensional systems. a computer program for transient and steady. National Technical Information Service, Bureau of Standards, Springfield .

Ferriz, H., Mahood, G., 1984. Eruption rates and compositional trends at los humeros volcanic center, puebla, mexico. journal of geophysical research. Solid Earth 89, 8511–8524.

Flores-Armenta, 2017. Inicio operación comercial los humeros iii fase a. "Geotermia, Revista Mexicana de Geoenergía" 30, 47–48.

Yáñez García, C., Casique-Velázquez, J., 1980. Informe geológico del proyecto geotérmico los humeros-las derrumbadas, estados de puenla y veracruz. Geotermia, Revista Mexicana de Geoenergía 15, 159–170.

Garduño-Monroy, V., Romero-Ríos, F., 1985. Análisis estructural del campo geotéérmico de los humeros, pue. CFE Internationl report 16, 539–554.

Giggenbach, W., 1988. Geothermal solute equilibria. derivation of na–k–mg–ca geoindicators.. ICosmochim 52, 2749–2765.

Glassley, William, E., 2015. Geothermal Energy, Renewable Energy and the Environment. CRC Press, 6000 Broken Sound Parkway NW, Suite 300.

Global-Energy-Observatory, 2018. Global power plant database. URL: https://datasets.wri.org/dataset/globalpowerplantdatabase.

González-Partida, E., Barragán-R., R., 1993. Ganállisis geoquímico-isotópico de las especies carbónicas del fluido deotérmico de los humeros, puebla, méxico. Geofísica internacional 32 No. 2, 299–309.

Grant Malcolm A., B.P.F., 2011. Geothermal Reservoir Engineering. Academic Press, University of California, Berkeley, California 94720.

Gutiérrez-Negrín, L., Izquierdo-Montalvo, G., 2010. Review and update of the main features of the los humeros geothermal field, mexico. World Geothermal Congress, Bali, Indonesia 7, 249–280.

Haukwa, C., 1998. AMESH, a mesh creating program for the integral finite difference method: A User's Manual. Report LBNL-45284, Earth Sciences Division, Lawrence Berkeley National Laboratory, University of California, Berkeley, CA 94720, USA. 53 p.

International-Formulation-Committee, 1967. Sa formulation of the thermodynamic properties of ordinary water substance. IFC Secretariat, Düsseldorf .

Izquierdo-Montalvo, G., Aragón-A, A., Portugal, E., 2008. Hydrothermal mineralogy as a tool to define the thermal aquifer of los humeros geothermal field, mexico. Geothermal Resources Council 32, 219–224.

Izquierdo-Montalvo, G., Gutiérrez-Negrín, L., 2009. Considerations on the origin of acid fluids in los humeros geothermal field, pue., mexico. GRC Trans. 33, 59–62.

López-Hernández, A., 1995. Estudio regiónal volcánico y estructural del campo de los humeros, puebla. Revista Mexicana de Geoenergía 11, 17–36.

Malate, R., O'Sullivan, M., 1992. Mathematical modelling of non–isothermal silica transport and deposition in a porous medium. Geothermics 21, 519–544.

McGuinness, M., Blakeley, M., Pruess, K., O'Sullivan, M., 1993. Geothermal heat pipe stability: solution selection by upstreaming and boundary conditions. Transport in Porous Media 11, 71–100.

Narasimhan, T., Witherspoon, P., 1976. An integrated finite difference method for analyzing. Fluid Flow in Porous Media 12, 57 – 64.

Norini, Groppelli, G., Sulpizio, R., 2015. Structural analysis and thermal remote sensing of the los humeros volcanic complex: Implications for volcano structure and geothermal exploration. Journal of Volcanology and Geothermal Research 301, 221–237.

O'Sullivan, J., Croucher, A., O'Sullivan, M., 2011. Modelling the evolution of a mine pit in a geothermal field at lihir island, papua new guinea. New Zealand geothermal workshop .

O'Sullivan, Michael, J., Pruess, K., Lippmann, Marcelo, J., 2001a. State of the art of geothermal reservoir simulation. Geothermics 30, 395–429.

O'Sullivan, M., Barnett, B., Razali, M., 1990. Numerical simulation of the kamojang geothermal field, indonesia. Transactions Geothermal Resources Council 14, 1317–1324.

O'Sullivan, M., Bullivant, D., Follows, S., 1998. Tauhara geothermal system. proceedings of the tough workshop 98. Berkeley, California 4, 1–6.

O'Sullivan, M., K, P., Lippmann, M., 2001b. State of the art of geothermal reservoir simulation. Geothermics 30, 395–429.

O'Sullivan, M., O'Sullivan, J., 2016. Reservoir modeling and simulation for geothermal resource characterization and evaluation. Elsevier.

O'Sullivan, M., Yeh, A., Mannington, W., 2009. A history of numerical modelling of wairakei geothermal field. Geothermics 38, 155–168.

Pritchett, J., Rice, M., Riney, T., 1981. Equation-of-state for water-carbon dioxide mixtures. implications for baca reservoir. Science and Software, La Joya CA. .

Program, S.G., 1980. Report: Sgp-tr42. Workshop on Geothermal Reservoir Engineering , 16–18.

Pruess, K., 1987. User's guide, nuclear regulatory commission report nureg/cr-4645. Lawrence Berkeley Laboratory Report LBL-20700 .

Pruess, K., Oldenburg, C., Moridis, G., 1999. TOUGH2 User's Guide, Version 2.0. Academic Press, 30 Corporate Drive, Suite 400, Burlington, MA 01803, USA.

R., G.N., Maya-González, 2015. Present situation and perspectives of geothermal in mexico. World Geothermal Congress 15, 19–25.

Ritchie, H., Roser, M., 2020. Renewable energy. Our World in Data Https://ourworldindata.org/renewable-energy.

Sanyal, S., 2002. A methodology for the assessment of geothermal energy reserves associated with volcanic systems. Geothermal Resources Council 26, 59–64.

Slack, K.a., 2009. Geothermal resources and climate emissions, geothermal energy association. Draft Report for Public Review , 1–117.

Solomon, S., Qin, M., Manning, Z., Chen, M., 2007. The physical science basis. contribution of working group i to the fourth assessment report of the intergovernmental panel on climate change. Cambridge University Press , 1–27.

Tello-Hinojosa, E., 1992. Caracteristicas geoquímicas e isotópicas de los fluídos producidos por los pozos de los humeros, pue., mexico. Revista Mexicana de Geoenergía 8 No.1, 3–48.

Torres-Rodríguez, M., 1992. Characterization of the reservoir of los humeros, mexico. Informe técnico para la comisión Federal de Electricidad 15 No.3, 1561–1566.

Tovar-Aguado, R., López-Romero, O., 1999. Comportamiento geoquímico e isotópico del fluído de los pozos del campo geotérmico los humeros, puebla, méxico. Revista Mexicana de Geoenergía 15 No.3, 171–181.

Uihlein, A., 2018. Jrc geothermal power plant dataset. URL: http://data.europa.eu/89h/jrc-10128-10001.

United-Nations, 2004. World population to 2300. united nations department of economic and social affairs, population division. Report ST/ESA/SER.A/236.

US-Energy-Administration, 2008. Renewable energy. Annual Energy Outlook U. S. Department of Energy Report DOE/EIA-0383 (2008).

Viggiano-Guerra, C., 1988. Control petrológico en el pozo h-26: sus posibilidades de producción. Revista Mexicana de Geoenergía 4 No.3, 123–138.

Viggiano-Guerra, C., Robles-Camacho, J., 1988. Mineralogía hidrotermal en el campo de los humero, pue. geometría del yacimiento. Revista Mexicana de Geoenergía 04 No. 1, 29–40.

Weir, G., White, S., 1996. Surface deposition from fluid flow in a porous medium. Transport in Porous Media 25, 79–96.

Zyvoloski, G., O'Sullivan, M., 1980. Simulation of a gas-dominated two-phase geothermal reservoir. Society of Petroleum Engineers Journal 20, 52–58.